An implicit G^1 multi patch B-Spline interpolation for Kirchhoff Love space rod

L. Greco[a], M. Cuomo[a,*]

[a]*Department of Civil and Environmental Engineering, University of Catania, viale A. Doria 6, 95100 Catania, Italy*

Abstract

The paper presents a novel formulation for the isogeometric analysis of assemblies of Kirchhoff-Love space rod elements, introducing a multi-patch implicit G^1 formulation, so that an automatic non-singular stiffness operator is obtained without the need of adding continuity conditions. The goal is achieved using a polar decomposition of the deformation of the first and last segments of the control polygon, that allows to introduce directly the end rotations as degrees of freedom. Both parametric and geometric continuity can be obtained in this way. We use Bezier and B-spline interpolations and we show that they are able to attain very good accuracy for developing a 3D exact curve element with geometric torsion (pre-twisted rod). In the paper the performance of the multi-patch elements is examined comparing the rates of convergence of the L^2 error norm for the multi-patch and single-patch formulations. It is shown that the rate of convergence remains the same, although in certain cases the accuracy is lower for the multi-patch solutions.

Keywords: Isogeometric analysis, B-splines, geometric continuity, multi patch analysis, Kirchhoff Love rod, curve rod element, pre-twisted rod element

1. Introduction

Structural theories for general curved and twisted space rods have been developed for polar and for non polar models (introducing the Kirchhoff-

*Corresponding author

Email addresses: leopoldo.greco@virgilio.it (L. Greco), mcuomo@unict.it (M. Cuomo)

Love hypotheses). Among the former essential contributions were given by Simo and Vu-Quoc[1], Simo[2], Crisfield[3]; in Luo[4] an essential bibliography on the subject can be found. A general model of non homogeneous composite and functionally graded curved space rods was contributed by Birsan et al.[5]. Kirchhoff-Love rods were extensively studied by Antman[6], and important contributions in the exact geometrical description of the motion were given by Langer and Singer[7], Ibrahimbegovic[8], among others. Shear undeformable rods with twist were used by Luongo et al.[9] to model the dynamics of flexible cables. We recall that in Kirchhoff theory a rod is considered as a space curve together with a rigid adaptive frame attached to it, to which is assigned a deformation energy accounting for axial, bending and torsional deformation (see, for instance, Bergou et al.[10], Jurdjevic[11]). Finite Element implementations of these models require special attention for the interpolation of the geometry, in order to guarantee the continuity of the intrinsic axes. In general, they exhibit jumps at the boundaries of the elements, that have to be smoothed in some way. In the context of standard polynomial interpolations many elements have been proposed for effectively treating this kind of structures, generally based on mixed or enhanced formulations (Simo and Vu-Quoc[1],Crisfield[3]). In Armero and Valverde[12] has been developed a C^1-continuous finite element based on Hermitian shape functions for the 2D plane case that has been successively extended to the 3D case in Armero and Valverde[13]. More recently, formulations that employ piecewise continuous interpolations on the elements and enforce inter-element continuity in a weak sense using the Discontinuous Galerkin approach have been proposed (Noels and Radovitzky[14]).

As opposite to the C^0 continuity obtained with the standard FEM discrete interpolations, isogeometric analysis, that employs B-splines (or NURBS), guarantees C^{p-1} continuity, (by means of the *blending* of the "shape functions" at the joints of the sections), p being the degree of the spline interpolation. Although B-spline functions are not shape functions in the usual sense, and they are not interpolatory they do verify the partition of unity, so in this work we shall refer to interpolation also for the B-spline discretization.

Thanks to the continuity property, isogeometric analysis represents a very appealing strategy for the numerical formulation of thin structural curved elements as rods and shells, since they can incorporate in the analysis the exact initial geometric curvatures without discontinuities. Indeed, isogeometric analysis allows a Galerkin's approach on exact geometry invariant under refinements. Isogeometric formulations of shell models have been an-

alyzed in Benson et al.[15] for polar and in Benson et al.[16], Kiendl et al.[17] and Kiendl et al.[18] for non polar shells. The application of B-spline interpolation to beams was investigated since the works of Gontier and Vollmer[19], who faced the large deformation problem, and Ganapathi et al.[20], who used cubic splines for eliminating locking. Application of isogeometric analysis to rods is more recent. Nagy et al.[21] used isogeometric analysis for the shape optimization of plane beams; Lu and Zhou[22] used Cosserat theory of rod allowing for cross sectional deformations of space curved rods, Bouclier et al.[23] and da Veiga et al.[24] proposed formulations for avoiding locking in curved plane Timoshenko beams. The high inter element continuity has been shown to be very effective for frequency analysis in Reali[25] and Cottrell et al.[26]. Recently, Greco and Cuomo[27] proposed a general non linear model for curved and twisted space rods based on Kirchhoff-Love hypotheses, and described its numerical implementation in an isogeometric framework. In it a parametrization of the cross section's directors independent from the *Frenet*'s triad was introduced by means of a decomposition of the rotation operator. Only the single patch case was examined.

Although B-spline interpolation presents C^{p-1} continuity in the interior, two adjacent patches can be joined only with C^0 continuity. In this way, in a Kirchhoff-Love approach that uses only displacements and torsional rotations as degrees of freedom, the global stiffness operator turns out to be singular. In order to avoid the singularity several strategies for enforcing the continuity conditions at the joints of the patches have been proposed by many authors, both for rods and non polar shells. In general, continuity conditions on the rotations are added to the formulation, that are equivalent to enforce the continuity of the unit tangent at the joints. This condition is known as geometric G^1 continuity, weaker than the parametric C^1 continuity. These continuity conditions in the CAD literature are known as the β-constraints and consist in constraint conditions for the positions of the control points (see Piegl and Tiller[28]). By means of the β-constraints geometric continuity of any degree may be imposed. In general this strategy is difficult for an automatic implementation.

On this line Bletzinger and Ramm[29] and successively Kiendl et al.[17] developed a strategy for an isogeometric G^1 multi-patch approach considering additional constraints for enforcing the alignment of the control points at the joints of the different patches. The same approach is adopted in Fisher et al.[30] for the analysis of 2D plane second gradient elasticity problems. A similar approach was presented by Greco[31] in which the constraints are

imposed directly on the unitary end tangents, i.e. on the rotations at the ends of the elements. Cottrell et al.[32], starting from consideration on the knots refinements, proposed a strategy for generating additional continuity conditions between patches with different number of control points at the boundary for 2D analyses.

Kiendl et al.[18], in order to overcome the necessity of the additional constraints and to obtain an easier automatic procedure for the assemblage of the global stiffness matrix introduce a relaxed G^1 constraint via the *bending strip methods*; this strategy is equivalent to a penalty methods. Similarly, Benson et al.[33] propose the concept of blended isogeometric shells for multi-patch analysis of polar and non polar shell elements.

Contrarily to the previous formulations, in the paper it is presented an implicit G^1 continuous Kirchhoff-Love rod element for the analysis of multi-patch assemblies of space rods; only *clamped*-B-splines interpolations are considered, see Piegl and Tiller[28], Farin[34] and Cottrell et al.[35]. Although in general a single patch can be used for modelling single beams, and degrees of freedom can be added increasing the number of internal knots, there are cases when it is necessary to discretise the rod element with more than one patch. Important examples are framed structures, composed by rods that are connected at the ends by rigid links requiring that the tangents keep their relative orientation during the deformation. Also in the cases of beams with sharply varying cross sections or in presence of point loads it may be useful the use of multiple patch interpolations. The strong (implicit) G^1 continuity is imposed by means of a re-parametrization of the second and second last control points of the centroid curve. By observing that for a *clamped* B-spline the direction of the tangent to the curve at the ends coincides with the directions of the first and last segments of the control polygon, the motion of these two segments is re-parametrized as a composition of a rigid rotation and a stretch (in this way a *polar decomposition* is obtained). Finally, adopting a spatial description for the rigid motions of the end directors, an automatic G^1 assemblage for the global stiffness is obtained.

The strong G^1 continuity conditions proposed in this work represents an extension of the Hermite interpolation to the isogeometric multi patch analyses. In the paper it is shown that in the case of a 3rd order Bezier interpolation, Hermite functions are exactly recovered. More general B-splines interpolations are also illustrated and are used in the applications.

The paper is organized as follows. In section 2 and 3 the Kirchhoff-Love space rod model already presented in Greco and Cuomo[27] is briefly revised.

With respect to the previous paper the formulation has been simplified and some additional information has been added on the rotation operators. In section 4 the proposed G^1 multi-patch interpolation is described in detail. Several applications are then discussed, aimed to compare the performance of the multi-patch approach with respect to the single patch model. It is shown that in general the rate of convergence of the L^2 error norm is the same for both approaches, although the accuracy is lower for the multi-patch case, but there are cases, specifically when discontinuous loads are present, for which the multi-patch model is more accurate. The application of the proposed methodology to two engineering applications of space grids complete the paper.

2. Space rod model

In this section it is given a short summary of the Kirchhoff-Love space rod model described in Greco and Cuomo[27]. The rod is defined by its axis and by the director vector lying in a plane orthogonal to it. The axis is a curve $\boldsymbol{p}(S) : \mathcal{A} \rightarrow \mathbb{R}^3$, where $\mathcal{A} =]0, L_0[$ is an open set of $\mathbb{R}$ and S is the arc-length of the Lagrangian configuration of the centroid axis. It is referred to a parametric abscissa λ defined in a certain interval $[0, a]$ The tangent vector to the rod axis is the vector field

$$\boldsymbol{t} = \frac{d\boldsymbol{p}}{dS} \tag{1}$$

The director vector is a unit vector field everywhere normal to the axis, $\boldsymbol{n}(S) : \mathcal{A} \rightarrow \mathbb{R}^3$.

2.1. Reference configuration

The original configuration is denoted by the index "0", so that in the unstrained configuration the unit tangent vector is (a hat denotes unit vectors)

$$\hat{\boldsymbol{t}}_0 = \frac{d\boldsymbol{p}_0}{dS} = \frac{1}{\|\boldsymbol{t}_0\|}\frac{d\boldsymbol{p}_0}{d\lambda}; \qquad \|\boldsymbol{t}_0\| = \frac{dS}{d\lambda} = \left\|\frac{d\boldsymbol{p}_0}{d\lambda}\right\| \tag{2}$$

Using (1) it results

$$\hat{\boldsymbol{t}} = \frac{1}{\|\boldsymbol{t}\|}\frac{d\boldsymbol{p}}{dS} = \frac{1}{\|\boldsymbol{t}\|}\frac{1}{\|\boldsymbol{t}_0\|}\frac{d\boldsymbol{p}}{d\lambda} \tag{3}$$

The description of the reference configuration of the rod is completed by the normal vector $\hat{\boldsymbol{n}}_0$. The orientation of the normal vector $\hat{\boldsymbol{n}}_0(S)$ is arbitrarily chosen (in the following it will be taken coincident with one of the principal inertia axes of the cross section). The unit local triad is completed by the unit vector

$$\hat{\boldsymbol{\nu}}_0(S) = \hat{\boldsymbol{t}}_0(S) \times \hat{\boldsymbol{n}}_0(S) \tag{4}$$

The (bending) curvature and torsion of the beam axis on the reference configuration are defined as:

$$\chi_{\nu 0} = -\frac{d\hat{\boldsymbol{n}}_0}{dS} \cdot \hat{\boldsymbol{t}}_0, \quad \chi_{n0} = \frac{d\hat{\boldsymbol{\nu}}_0}{dS} \cdot \hat{\boldsymbol{t}}_0, \quad \chi_{t0} = \frac{d\hat{\boldsymbol{n}}_0}{dS} \cdot \hat{\boldsymbol{\nu}}_0. \tag{5}$$

Introducing the abscissas θ^n, θ^ν along the normal vectors, the initial position of a generic point of the beam is:

$$\overset{*}{\boldsymbol{p}}_0 = \boldsymbol{p}_0 + \theta^n \hat{\boldsymbol{n}}_0 + \theta^\nu \hat{\boldsymbol{\nu}}_0 \tag{6}$$

2.2. Kinematics of the Kirchhoff Love rod

The current position of the centroid curve is given by

$$\boldsymbol{p}(S) = \boldsymbol{p}_0(S) + \boldsymbol{u}(S), \tag{7}$$

Differently from what is done in Langer and Singer[7], the rotation of the cross section is given by two isometric operators, $\boldsymbol{\Lambda}(\hat{\boldsymbol{t}}_0(S), \hat{\boldsymbol{t}}(S))$, a rotation without drilling rotation that rotates the vector $\hat{\boldsymbol{t}}_0(S)$ on $\hat{\boldsymbol{t}}(S)$, and $\boldsymbol{R}(\hat{\boldsymbol{t}}(S), \phi(S))$ that gives the drilling rotation $\phi(S) : [0, L_0] \to \mathbb{R}$ around $\hat{\boldsymbol{t}}(S)$. This rotation will be also referred to as correction angle. The two operators are obtained particularizing *Euler-Rodrigues* formula

$$\boldsymbol{\mathfrak{R}} = \hat{\boldsymbol{e}} \otimes \hat{\boldsymbol{e}} + \cos[\varphi](\boldsymbol{I} - \hat{\boldsymbol{e}} \otimes \hat{\boldsymbol{e}}) + \sin[\varphi]\hat{\boldsymbol{e}} \times \boldsymbol{I}. \tag{8}$$

where $\hat{\boldsymbol{e}}$ is the axis of rotation, while φ is the angle of rotation.

The unitary axial vector of the first rotation is $\hat{\boldsymbol{e}} = \frac{\hat{\boldsymbol{t}}_0 \times \hat{\boldsymbol{t}}}{\|\hat{\boldsymbol{t}}_0 \times \hat{\boldsymbol{t}}\|}$ while $\cos[\varphi] = \hat{\boldsymbol{t}}_0 \cdot \hat{\boldsymbol{t}}$ and $\sin[\varphi] = \|\hat{\boldsymbol{t}}_0 \times \hat{\boldsymbol{t}}\|$, therefore the formula (8) gives the representation

$$\boldsymbol{\Lambda}(\hat{\boldsymbol{t}}_0, \hat{\boldsymbol{t}}) = (\hat{\boldsymbol{t}}_0 \cdot \hat{\boldsymbol{t}})\boldsymbol{I} + \left(\hat{\boldsymbol{t}}_0 \times \hat{\boldsymbol{t}}\right) \times \boldsymbol{I} + \frac{1}{1 + \hat{\boldsymbol{t}}_0 \cdot \hat{\boldsymbol{t}}}(\hat{\boldsymbol{t}}_0 \times \hat{\boldsymbol{t}}) \otimes (\hat{\boldsymbol{t}}_0 \times \hat{\boldsymbol{t}}) \tag{9}$$

.

The axial vector of the second rotation operator is $\hat{\boldsymbol{e}} = \hat{\boldsymbol{t}}$, and indicating the correction angle by ϕ, equation (8) gives

$$\boldsymbol{R}(\hat{\boldsymbol{t}},\phi) = \boldsymbol{I} + \sin[\phi]\,\hat{\boldsymbol{t}}\times\boldsymbol{I} + (1-\cos[\phi])\,\hat{\boldsymbol{t}}\times\left(\hat{\boldsymbol{t}}\times\boldsymbol{I}\right). \tag{10}$$

.

The normal axes of the local triad are then

$$\hat{\boldsymbol{n}}(S) = \boldsymbol{Q}\hat{\boldsymbol{n}}_0(S), \quad \hat{\boldsymbol{\nu}}(S) = \boldsymbol{Q}\hat{\boldsymbol{\nu}}_0(S), \quad \boldsymbol{Q} = \boldsymbol{R}(\hat{\boldsymbol{t}},\phi)\boldsymbol{\Lambda}(\hat{\boldsymbol{t}}_0,\hat{\boldsymbol{t}}). \tag{11}$$

The construction described satisfies Kirchhoff-Love hypotheses $\hat{\boldsymbol{t}}\cdot\hat{\boldsymbol{n}} = \hat{\boldsymbol{t}}\cdot\hat{\boldsymbol{\nu}} = 0$. We observe that the (Lagrangian) description of the deformed configuration of the rod is defined by means of the two fields $\{\boldsymbol{u}(S),\phi(S)\}$, so that it has four degrees of freedom.

It is possible to give a matrix representation of the operators $\boldsymbol{R},\boldsymbol{\Lambda}$, that are elements of the group SO^3. In the material frame the operator $\boldsymbol{\Lambda}$ assumes the form

$$\boldsymbol{\Lambda} = \begin{pmatrix} \hat{\boldsymbol{t}}\cdot\hat{\boldsymbol{t}}_0 & -\hat{\boldsymbol{t}}\cdot\hat{\boldsymbol{n}}_0 & -\hat{\boldsymbol{t}}\cdot\hat{\boldsymbol{\nu}}_0 \\ \hat{\boldsymbol{t}}\cdot\hat{\boldsymbol{n}}_0 & \hat{\boldsymbol{t}}\cdot\hat{\boldsymbol{t}}_0 + \frac{\left(\hat{\boldsymbol{t}}\cdot\hat{\boldsymbol{\nu}}_0\right)^2}{1+\hat{\boldsymbol{t}}\cdot\hat{\boldsymbol{t}}_0} & +\frac{\left(\hat{\boldsymbol{t}}\cdot\hat{\boldsymbol{n}}_0\right)\left(\hat{\boldsymbol{t}}\cdot\hat{\boldsymbol{\nu}}_0\right)}{1+\hat{\boldsymbol{t}}\cdot\hat{\boldsymbol{t}}_0} \\ \hat{\boldsymbol{t}}\cdot\hat{\boldsymbol{\nu}}_0 & -\frac{\left(\hat{\boldsymbol{t}}\cdot\hat{\boldsymbol{n}}_0\right)\left(\hat{\boldsymbol{t}}\cdot\hat{\boldsymbol{\nu}}_0\right)}{1+\hat{\boldsymbol{t}}\cdot\hat{\boldsymbol{t}}_0} & \hat{\boldsymbol{t}}\cdot\hat{\boldsymbol{t}}_0 + \frac{\left(\hat{\boldsymbol{t}}\cdot\hat{\boldsymbol{n}}_0\right)^2}{1+\hat{\boldsymbol{t}}\cdot\hat{\boldsymbol{t}}_0} \end{pmatrix} \tag{12}$$

while the isometry $\boldsymbol{R}$ is more effectively represented in the intermediate spatial frame $\{\hat{\boldsymbol{t}},\hat{\boldsymbol{n}}^\flat = \boldsymbol{\Lambda}\hat{\boldsymbol{n}}_0,\hat{\boldsymbol{\nu}}^\flat = \boldsymbol{\Lambda}\hat{\boldsymbol{\nu}}_0\}$,

$$\boldsymbol{R} = \begin{pmatrix} 1 & 0 & 0 \\ 0 & \cos(\phi) & -\sin(\phi) \\ 0 & \sin(\phi) & \cos(\phi) \end{pmatrix} \tag{13}$$

The position of a generic point in the cross section is identified by the vector

$$\overset{*}{\boldsymbol{p}}(S,\vartheta^n,\vartheta^\nu) = \boldsymbol{p}(S) + \boldsymbol{\xi} = \boldsymbol{p}(S) + \vartheta^n\hat{\boldsymbol{n}}(S) + \vartheta^\nu\hat{\boldsymbol{\nu}}(S). \tag{14}$$

The tangent vectors at the generic fibre of the rod are obtained differentiating equation (14)

$$\overset{*}{\boldsymbol{t}} := \frac{\partial\overset{*}{\boldsymbol{p}}}{\partial S} = \frac{\partial\boldsymbol{p}}{\partial S} + \vartheta^\nu\frac{\partial\hat{\boldsymbol{\nu}}}{\partial S} + \vartheta^n\frac{\partial\hat{\boldsymbol{n}}}{\partial S}, \quad \overset{*}{\boldsymbol{n}} := \frac{\partial\overset{*}{\boldsymbol{p}}}{\partial\vartheta^n} = \hat{\boldsymbol{n}}, \quad \overset{*}{\boldsymbol{\nu}} := \frac{\partial\overset{*}{\boldsymbol{p}}}{\partial\vartheta^\nu} = \hat{\boldsymbol{\nu}} \tag{15}$$

Indicating with the apex $\natural$ the contravariant basis, the metric of the spatial configuration is

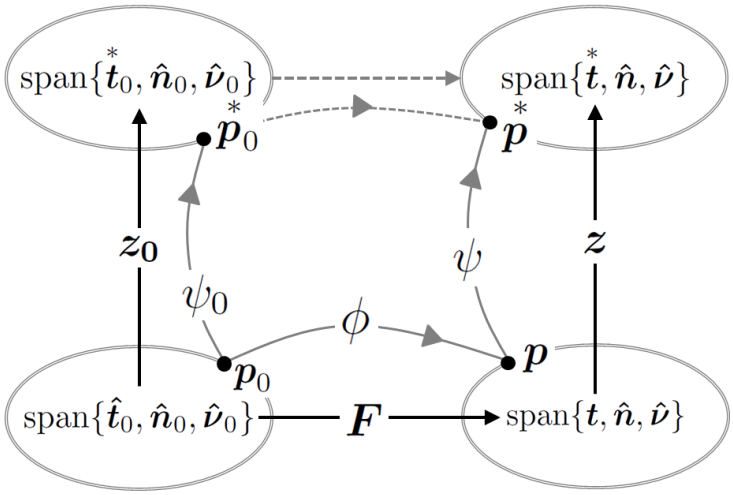

Figure 1: Tangent spaces and relate tangent operators.

$$\overset{*}{\mathcal{G}} = \overset{*}{\boldsymbol{t}} \otimes \overset{*\natural}{\boldsymbol{t}} + \hat{\boldsymbol{n}} \otimes \overset{*\natural}{\boldsymbol{n}} + \hat{\boldsymbol{\nu}} \otimes \overset{*\natural}{\boldsymbol{\nu}} \tag{16}$$

and the metric of the reference configuration is

$$\overset{*}{\mathcal{G}}_0 = \overset{*}{\boldsymbol{t}}_0 \otimes \overset{*\natural}{\boldsymbol{t}}_0 + \hat{\boldsymbol{n}}_0 \otimes \overset{*\natural}{\boldsymbol{n}}_0 + \hat{\boldsymbol{\nu}}_0 \otimes \overset{*\natural}{\boldsymbol{\nu}}_0 \tag{17}$$

All the state variables are referred to the centroid line, using the pull back operators of the maps ψ_0, ψ from the centroid line of the rod to the generic fibre, defined in fig. 1.

$$\begin{aligned} \boldsymbol{z} =& \overset{*}{\boldsymbol{g}}_\alpha \otimes \boldsymbol{g}^\alpha,\ \overset{*}{\boldsymbol{g}}_\alpha = \{\overset{*}{\boldsymbol{t}}, \hat{\boldsymbol{n}}, \hat{\boldsymbol{\nu}}\},\ \boldsymbol{g}^\alpha = \{\boldsymbol{t}^\natural, \hat{\boldsymbol{n}}, \hat{\boldsymbol{\nu}}\} \\ \boldsymbol{z}_0 =& \overset{*}{\boldsymbol{g}}_{0\alpha} \otimes \boldsymbol{g}_0^\alpha,\ \overset{*}{\boldsymbol{g}}_{0\alpha} = \{\overset{*}{\boldsymbol{t}}_0, \hat{\boldsymbol{n}}_0, \hat{\boldsymbol{\nu}}_0\},\ \boldsymbol{g}_0^\alpha = \{\hat{\boldsymbol{t}}_0, \hat{\boldsymbol{n}}_0, \hat{\boldsymbol{\nu}}_0\} \end{aligned} \tag{18}$$

Denoting with $\boldsymbol{F}$ the gradient of deformation from the reference configuration of the axis to its current configuration i.e. $\boldsymbol{F} = \boldsymbol{g}_\alpha \otimes \boldsymbol{g}_0^\alpha = \boldsymbol{t} \otimes \hat{\boldsymbol{t}}_0 + \hat{\boldsymbol{n}} \otimes \hat{\boldsymbol{n}}_0 + \hat{\boldsymbol{\nu}} \otimes \hat{\boldsymbol{\nu}}_0$ the strain tensor is the difference between the pull back of $\overset{*}{\mathcal{G}}$ on the tangent space to the reference configuration of the rod axis, $\phi^* \left(\psi^* (\overset{*}{\mathcal{G}}) \right) = \boldsymbol{F}^T \boldsymbol{z}^T \overset{*}{\mathcal{G}} \boldsymbol{z} \boldsymbol{F}$, and the pull back on the same tangent space of the material metric, $\boldsymbol{z}_0^T \overset{*}{\mathcal{G}}_0 \boldsymbol{z}_0$, i.e.,

$$\boldsymbol{E} = \frac{1}{2}\left(\phi^*\left(\psi^*(\overset{*}{\mathcal{G}})\right) - \psi_0^*(\overset{*}{\mathcal{G}}_0)\right) \tag{19}$$

The components of the first tensor on the triad $\{\hat{\boldsymbol{t}}_0, \hat{\boldsymbol{n}}_0, \hat{\boldsymbol{\nu}}_0\}$ are, after enforcing the Kirchhoff-Love constraints,

$$\phi^*\left(\psi^*(\overset{*}{\mathcal{G}})\right) = \begin{pmatrix} \overset{*}{\boldsymbol{t}} \cdot \overset{*}{\boldsymbol{t}} & -\vartheta^\nu\left(\frac{d\hat{\boldsymbol{n}}}{dS}\cdot\hat{\boldsymbol{\nu}}\right) & \vartheta^n\left(\frac{d\hat{\boldsymbol{n}}}{dS}\cdot\hat{\boldsymbol{\nu}}\right) \\ -\vartheta^\nu\left(\frac{d\hat{\boldsymbol{n}}}{dS}\cdot\hat{\boldsymbol{\nu}}\right) & 1 & 0 \\ \vartheta^n\left(\frac{d\hat{\boldsymbol{n}}}{dS}\cdot\hat{\boldsymbol{\nu}}\right) & 0 & 1 \end{pmatrix} \tag{20}$$

The pull back of the material metric is, analogously,

$$\psi_0^*(\overset{*}{\mathcal{G}}) = \begin{pmatrix} \overset{*}{\boldsymbol{t}}_0 \cdot \overset{*}{\boldsymbol{t}}_0 & -\vartheta^\nu\left(\frac{d\hat{\boldsymbol{n}}_0}{dS}\cdot\hat{\boldsymbol{\nu}}_0\right) & \vartheta^n\left(\frac{d\hat{\boldsymbol{n}}_0}{dS}\cdot\hat{\boldsymbol{\nu}}_0\right) \\ -\vartheta^\nu\left(\frac{d\hat{\boldsymbol{n}}_0}{dS}\cdot\hat{\boldsymbol{\nu}}_0\right) & 1 & 0 \\ \vartheta^n\left(\frac{d\hat{\boldsymbol{n}}_0}{dS}\cdot\hat{\boldsymbol{\nu}}_0\right) & 0 & 1 \end{pmatrix} \tag{21}$$

In the expressions (20) (21) it is possible to recognize the initial curvatures and torsion, defined in (5) and the spatial curvatures and torsion, similarly defined as

$$\chi_\nu = -\frac{d\hat{\boldsymbol{n}}}{dS}\cdot\boldsymbol{t},\ \chi_n = \frac{d\hat{\boldsymbol{\nu}}}{dS}\cdot\boldsymbol{t},\ \chi_t = \frac{d\hat{\boldsymbol{n}}}{dS}\cdot\hat{\boldsymbol{\nu}}. \tag{22}$$

The strain tensor is then written as

$$\boldsymbol{E} = \frac{1}{2}\begin{pmatrix} \overset{*}{\boldsymbol{t}}\cdot\overset{*}{\boldsymbol{t}} - \hat{\boldsymbol{t}}_0\cdot\hat{\boldsymbol{t}}_0 & -\vartheta^\nu\left(\chi_t - \chi_{t0}\right) & \vartheta^n\left(\chi_t - \chi_{t0}\right) \\ -\vartheta^\nu\left(\chi_t - \chi_{t0}\right) & 0 & 0 \\ \vartheta^n\left(\chi_t - \chi_{t0}\right) & 0 & 0 \end{pmatrix} \tag{23}$$

with

$$\begin{aligned} \overset{*}{\boldsymbol{t}}\cdot\overset{*}{\boldsymbol{t}} - \hat{\boldsymbol{t}}_0\cdot\hat{\boldsymbol{t}}_0 =& \|\boldsymbol{t}\|^2 - 1 - 2\vartheta^n\left(\chi_\nu - \chi_{\nu 0}\right) + 2\vartheta^\nu\left(\chi_n - \chi_{n0}\right) \\ &+ \dots \end{aligned} \tag{24}$$

having disregarded quadratic terms in $\vartheta^n, \vartheta^\nu$.

2.3. Tangent operator

The velocity of a generic point of the beam is

$$\dot{\overset{*}{\boldsymbol{p}}} = \dot{\boldsymbol{u}} + \vartheta^n \dot{\hat{\boldsymbol{n}}} + \vartheta^\nu \dot{\hat{\boldsymbol{\nu}}} \tag{25}$$

The velocity of the intrinsic triad is given by

$$\{\hat{\boldsymbol{t}}, \hat{\boldsymbol{n}}, \hat{\boldsymbol{\nu}}\} = \boldsymbol{Q}\{\hat{\boldsymbol{t}}_0, \hat{\boldsymbol{n}}_0, \hat{\boldsymbol{\nu}}_0\} \Rightarrow \{\dot{\hat{\boldsymbol{t}}}, \dot{\hat{\boldsymbol{n}}}, \dot{\hat{\boldsymbol{\nu}}}\} = \dot{\boldsymbol{Q}}\{\hat{\boldsymbol{t}}_0, \hat{\boldsymbol{n}}_0, \hat{\boldsymbol{\nu}}_0\} = \dot{\boldsymbol{Q}}\boldsymbol{Q}^{-1}\{\hat{\boldsymbol{t}}, \hat{\boldsymbol{n}}, \hat{\boldsymbol{\nu}}\} \tag{26}$$

We get:

$$\dot{\hat{\boldsymbol{n}}} = \lim_{d\tau \to 0} \frac{\hat{\boldsymbol{n}}(\tau + d\tau) - \hat{\boldsymbol{n}}(\tau)}{d\tau} = \lim_{d\tau \to 0} \frac{\left(\boldsymbol{Q}_\tau^{\tau+d\tau} - \boldsymbol{I}\right) \hat{\boldsymbol{n}}(\tau)}{d\tau} \tag{27}$$

where $\boldsymbol{Q}_\tau^{\tau+d\tau}$ is the rotation operator from the configuration at time τ to the configuration at time $\tau+d\tau$, given by $\boldsymbol{Q}_\tau^{\tau+d\tau} = \boldsymbol{R}\left(\hat{\boldsymbol{t}}(\tau + d\tau), \phi(\tau + d\tau)\right) \boldsymbol{\Lambda}\left(\boldsymbol{t}(\tau), \boldsymbol{t}(\tau + d\tau)\right)$, that can be evaluated using formulas (9), (10). By direct evaluation it is found that

$$\dot{\boldsymbol{Q}}\boldsymbol{Q}^T = \boldsymbol{R}\dot{\boldsymbol{\Lambda}}\boldsymbol{\Lambda}^T\boldsymbol{R}^T + \dot{\boldsymbol{R}}\boldsymbol{R}^T = \left(\dot{\hat{\boldsymbol{t}}} \otimes \hat{\boldsymbol{t}} - \hat{\boldsymbol{t}} \otimes \dot{\hat{\boldsymbol{t}}}\right) + \dot{\phi}\, \hat{\boldsymbol{t}} \times \boldsymbol{I}. \tag{28}$$

The axial vector $\boldsymbol{\omega}(S) : [0, L_0] \to \mathbb{R}^3$ associated to $\dot{\boldsymbol{Q}}\boldsymbol{Q}^T$ is:

$$\boldsymbol{\omega} = \dot{\phi}\hat{\boldsymbol{t}} + \omega_n \hat{\boldsymbol{n}} + \omega_\nu \hat{\boldsymbol{\nu}} \tag{29}$$

with

$$\omega_n = \dot{\hat{\boldsymbol{\nu}}} \cdot \hat{\boldsymbol{t}} = -\frac{1}{\|\boldsymbol{t}\|}\frac{d\dot{\boldsymbol{u}}}{dS} \cdot \hat{\boldsymbol{\nu}}; \quad \omega_\nu = -\dot{\hat{\boldsymbol{n}}} \cdot \hat{\boldsymbol{t}} = \frac{1}{\|\boldsymbol{t}\|}\frac{d\dot{\boldsymbol{u}}}{dS} \cdot \hat{\boldsymbol{n}}. \tag{30}$$

where the identities $\dot{\hat{\boldsymbol{\nu}}} \cdot \hat{\boldsymbol{t}} = -\hat{\boldsymbol{\nu}} \cdot \dot{\hat{\boldsymbol{t}}}$ and $\dot{\hat{\boldsymbol{n}}} \cdot \hat{\boldsymbol{t}} = -\hat{\boldsymbol{n}} \cdot \dot{\hat{\boldsymbol{t}}}$, consequences of Kirchhoff-Love constraints, have been used.

With the aid of the axial vector $\boldsymbol{\omega}$, the velocity of the intrinsic triad takes the form

$$\begin{aligned} \dot{\hat{\boldsymbol{t}}} &= \omega \times \hat{\boldsymbol{t}} = \omega_\nu \hat{\boldsymbol{n}} - \omega_n \hat{\boldsymbol{\nu}} \\ \dot{\hat{\boldsymbol{n}}} &= \omega \times \hat{\boldsymbol{n}} = -\omega_\nu \hat{\boldsymbol{t}} + \dot{\phi}\hat{\boldsymbol{\nu}} \\ \dot{\hat{\boldsymbol{\nu}}} &= \omega \times \hat{\boldsymbol{\nu}} = \omega_n \hat{\boldsymbol{t}} - \dot{\phi}\hat{\boldsymbol{n}}. \end{aligned} \tag{31}$$

We observe, for later use, that the continuity of the beam is guaranteed if the velocities of the torsional rotation $\dot{\phi}$ and of the bending rotations ω_n, ω_ν are continuous.

2.4. The velocity of deformation operator for a Kirchhoff-Love rod

In this section we derive the velocity of deformation tensor. Its form is the same as the infinitesimal deformation tensor that will be used in the applications.

The pull-back of the velocity of deformation on the reference configuration $\dot{\boldsymbol{E}} = \dot{E}_{\alpha\beta}\, \boldsymbol{g}_0^\alpha \otimes \boldsymbol{g}_0^\beta = sym\left((\boldsymbol{z}\boldsymbol{F})^T \dot{\boldsymbol{z}}\boldsymbol{F}\right)$ has the components (see equation (23))

$$\dot{\boldsymbol{E}} = \frac{1}{2}\begin{pmatrix} 2\,\overset{\dot{*}}{\boldsymbol{t}} \cdot \overset{*}{\boldsymbol{t}} & -\vartheta^\nu \dot{\chi}_t & \vartheta^n \dot{\chi}_t \\ -\vartheta^\nu \dot{\chi}_t & 0 & 0 \\ \vartheta^n \dot{\chi}_t & 0 & 0 \end{pmatrix} \tag{32}$$

The components of the tensor $\dot{\boldsymbol{E}}$ are readily found performing the derivatives in (32). The axial component of the velocity of deformation of the generic fibre is

$$\overset{\dot{*}}{\boldsymbol{t}} \cdot \overset{*}{\boldsymbol{t}} = \dot{\varepsilon} + \hat{\boldsymbol{t}} \times \dot{\boldsymbol{\chi}} \cdot \boldsymbol{\xi} \tag{33}$$

with

$$\dot{\varepsilon} = \dot{\boldsymbol{t}} \cdot \boldsymbol{t} \tag{34}$$

$$\hat{\boldsymbol{t}} \times \dot{\boldsymbol{\chi}} = -\dot{\chi}_\nu \hat{\boldsymbol{n}} + \dot{\chi}_n \hat{\boldsymbol{\nu}} \tag{35}$$

$$\boldsymbol{\xi} = \vartheta^n \hat{\boldsymbol{n}} + \vartheta^\nu \hat{\boldsymbol{\nu}} \tag{36}$$

having disregarded terms of order higher than 1 in $\vartheta^n, \vartheta^\nu$. The velocities of the curvatures are evaluated as follows:

$$\dot{\chi}_t = \frac{d\dot{\hat{\boldsymbol{n}}}}{dS} \cdot \hat{\boldsymbol{\nu}} + \frac{d\hat{\boldsymbol{n}}}{dS} \cdot \dot{\hat{\boldsymbol{\nu}}} = \frac{d\boldsymbol{\omega}}{dS} \cdot \hat{\boldsymbol{t}} \tag{37}$$

$$\dot{\chi}_n = \frac{d\dot{\hat{\boldsymbol{\nu}}}}{dS} \cdot \boldsymbol{t} + \frac{d\hat{\boldsymbol{\nu}}}{dS} \cdot \dot{\boldsymbol{t}} = \frac{d\boldsymbol{\omega}}{dS} \cdot \hat{\boldsymbol{n}}\|\boldsymbol{t}\| + \dot{\boldsymbol{t}} \cdot \boldsymbol{t} \frac{1}{\|\boldsymbol{t}\|^2} \chi_n \tag{38}$$

$$\dot{\chi}_\nu = -\left(\frac{d\dot{\hat{\boldsymbol{n}}}}{dS} \cdot \boldsymbol{t} + \frac{d\hat{\boldsymbol{n}}}{dS} \cdot \dot{\boldsymbol{t}}\right) = \frac{d\boldsymbol{\omega}}{dS} \cdot \hat{\boldsymbol{\nu}}\|\boldsymbol{t}\| + \dot{\boldsymbol{t}} \cdot \boldsymbol{t} \frac{1}{\|\boldsymbol{t}\|^2} \chi_\nu \tag{39}$$

The generalized deformation (34), (37), (38), (39) can be related to the degrees of freedom of the rod accounting for Kirchhoff-Love constraints. Recalling from (29) that $\boldsymbol{\omega} = \dot{\phi}\hat{\boldsymbol{t}} + \frac{1}{\|\boldsymbol{t}\|}\hat{\boldsymbol{t}} \times \frac{d\dot{\boldsymbol{u}}}{dS}$ and evaluating its gradient:

$$\frac{d\boldsymbol{\omega}}{dS} = \frac{d\dot{\phi}}{dS} + \dot{\phi}\frac{d\hat{\boldsymbol{t}}}{dS} + \frac{1}{\|\boldsymbol{t}\|}\frac{d\hat{\boldsymbol{t}}}{dS} \times \frac{d\dot{\boldsymbol{u}}}{dS} + \hat{\boldsymbol{t}} \times \frac{d}{dS}\left(\frac{1}{\|\boldsymbol{t}\|}\frac{d\dot{\boldsymbol{u}}}{dS}\right), \tag{40}$$

noting that

$$\hat{\boldsymbol{t}} \times \frac{d\hat{\boldsymbol{t}}}{dS} = \frac{1}{\|\boldsymbol{t}\|}\left(\chi_n\hat{\boldsymbol{n}} + \chi_\nu\hat{\boldsymbol{\nu}}\right) = \frac{1}{\|\boldsymbol{t}\|}\boldsymbol{\chi}_b \tag{41}$$

where $\boldsymbol{\chi}_b = \left(\boldsymbol{I} - \hat{\boldsymbol{t}} \otimes \hat{\boldsymbol{t}}\right)\boldsymbol{\chi}$ and introducing the second line covariant derivative of $\dot{\boldsymbol{u}}$ that is defined as

$$\dot{\boldsymbol{u}}_{|S|S} = \|\boldsymbol{t}\|\frac{d}{dS}\left(\frac{1}{\|\boldsymbol{t}\|}\frac{d\dot{\boldsymbol{u}}}{dS}\right) \tag{42}$$

we have the results:

$$\dot{\chi}_t = \frac{d\boldsymbol{\omega}}{dS} \cdot \hat{\boldsymbol{t}} = \frac{d\dot{\phi}}{dS} + \frac{1}{\|\boldsymbol{t}\|^2}\boldsymbol{\chi}_b \cdot \frac{d\dot{\boldsymbol{u}}}{dS} \tag{43}$$

$$\hat{\boldsymbol{t}} \times \dot{\boldsymbol{\chi}} = \dot{\phi}\boldsymbol{\chi}_b - \left(\boldsymbol{I} - \hat{\boldsymbol{t}} \otimes \hat{\boldsymbol{t}}\right)\dot{\boldsymbol{u}}_{\|S\|S} \tag{44}$$

3. Equilibrium operator for *Kirchhoff-Love* rod

3.1. Virtual Power Identity

Let's denote by $\boldsymbol{S} = S^{\alpha\beta}\boldsymbol{g}_{0\alpha}\boldsymbol{g}_{0\beta}$ the second Piola Kirchhoff stress tensor, given by the pull back of the Cauchy stress tensor at the generic fiber $\overset{*}{\boldsymbol{\Sigma}}$ as follows

$$\boldsymbol{S} = \det(\boldsymbol{zF})(\boldsymbol{zF})^{-1}\overset{*}{\boldsymbol{\Sigma}}(\boldsymbol{zF})^{-T} \tag{45}$$

Introducing the hypotheses of plane stress, its components on the reference unitary centroid triads are

$$S = \begin{pmatrix} S^{tt} & S^{tn} & S^{t\nu} \\ S^{nt} & 0 & 0 \\ S^{\nu t} & 0 & 0 \end{pmatrix}. \tag{46}$$

The Lagrangian form of the internal virtual power is

$$P_{int} = \int_{L_0} \int_{\mathcal{A}} \left[S^{tt}(\dot{\varepsilon} - \vartheta^n \dot{\chi}_\nu + \vartheta^\nu \dot{\chi}_n) + (S^{t\nu}\vartheta^n - S^{tn}\vartheta^\nu)\dot{\chi}_t \right] d\mathcal{A}\, dS \tag{47}$$

Substituting the components of the velocity of deformation, expressions (34), (37), (38), (39) and assembling the terms, it becomes

$$P_{int} = \int_{L_0} \left(N + M_n \frac{\chi_n}{\|\boldsymbol{t}\|^3} + M_\nu \frac{\chi_\nu}{\|\boldsymbol{t}\|^3} \right) \boldsymbol{t} \cdot \dot{\boldsymbol{t}} + \boldsymbol{M} \cdot \frac{d\boldsymbol{\omega}}{dS}\, dS \tag{48}$$

having introduced the definitions:

$$\begin{aligned} N &= \int_{\mathcal{A}} S^{tt} d\mathcal{A} \\ M_t &= \int_{\mathcal{A}} (S^{t\nu}\vartheta^n - S^{tn}\vartheta^\nu)\, d\mathcal{A} \\ M_n &= \int_{\mathcal{A}} S^{tt}\vartheta^\nu \|\boldsymbol{t}\|\, d\mathcal{A} \\ M_\nu &= -\int_{\mathcal{A}} S^{tt}\vartheta^n \|\boldsymbol{t}\|\, d\mathcal{A} \\ \boldsymbol{M} &= (M_t, M_n, M_\nu)\,. \end{aligned} \tag{49}$$

The internal stress resultant dual to the axial deformation is the effective axial force

$$N_{eff} = N + M_n \frac{\chi_n}{\|\boldsymbol{t}\|^3} + M_\nu \frac{\chi_\nu}{\|\boldsymbol{t}\|^3} \tag{50}$$

In the computation, however, it is more convenient to use the expressions (43), (44) for computing the internal power, since the velocities are normally referred to an external cartesian frame. The relevant expression is straightforward and is not reported here.

3.2. Constitutive operator of the rod

We assume that the rod remains elastic, and denote by

$$\dot{\boldsymbol{S}} = \mathbb{C}_t : \dot{\boldsymbol{E}} \tag{51}$$

the tangent constitutive relationship between the increment of the second Piola-Kirchhoff stress tensor and the convective velocity of deformation. In this work we employ the approximation that the tangent elastic coefficients be constant, and according to Simo[2], Kiendl et al.[18], we assume that

$$\begin{aligned} \dot{S}^{tt} &= E\,(\overset{*}{\dot{\boldsymbol{t}}} \cdot \overset{*}{\boldsymbol{t}}) = E\,(\dot{\varepsilon} - \vartheta^n \dot{\chi}_\nu + \vartheta^\nu \dot{\chi}_n) \\ \dot{S}^{tn} &= -G\,\vartheta^\nu\,\dot{\chi}_t \quad \dot{S}^{t\nu} = G\,\vartheta^n\,\dot{\chi}_t. \end{aligned} \tag{52}$$

Proceeding as in Greco and Cuomo[27], Cuomo and Greco[36] the material stiffness matrix can be obtained. It is the sum of four contributions (membrane, torsional, and two bending contributions), and strong coupling is present between the displacement degrees of freedom and the torsional rotation.

4. Interpolation

A B-spline interpolation is used for the rod configuration $(\boldsymbol{p}, \phi)(S)$. For the sake of completeness we recall that a B-spline curve of degree p is defined as

$$\mathbf{C}(\lambda) = \sum_{i=1}^{n} b_i^p(\lambda)\mathbf{P}_i \tag{53}$$

where $\mathbf{P}_i = \{P_{ix}, P_{iy}, P_{iz}\}$ are the cartesian components of n control points, and $b_i^p(\lambda)$ are n B-spline basis functions of degree p defined on a non periodic knot vector. The knot vector is a non decreasing sequence of m real numbers, corresponding to the parametric coordinates $\lambda_j, j = 1, ..., m$, with $m = n + p + 1$,

$$\Xi = \{\underbrace{a, ..., a}_{p+1}, \underbrace{\lambda_{p+2}, ..., \lambda_{m-(p+2)}}_{m-2(p+1)}, \underbrace{b, ..., b}_{p+1}\}$$

The global interval $[a, b]$ is called the patch. In this work non periodic open knot vectors are considered, with multiplicity equal to 1 for each internal knot, that ensures a C^{p-1} parametric continuity at each knot. Increasing the multiplicity of a knot corresponds to reducing by one the continuity degree. Open b-splines are such that the first and last knots in Ξ have multiplicity

$p+1$, so that continuity is lost at the ends of the patch. Since B-splines are interpolatory for the first and last control points, two patches can be joined matching the coordinates of the control point at the common end, but only C^0 continuity is obtained.

If in the knot vector there is no internal knot the basis functions reduce to the Bernstein polynomials, so that the B-spline interpolation is a generalization of the Bezier's interpolation. In this work both Bezier and general B-spline interpolation will be used. An interesting property of the B-spline interpolation of a curve with an open knot vector is that the interpolated curve is tangential to the control polygon at the ends.

4.1. Single patch interpolation

We adopt for the representation of the rod configuration of the centroid axis of the rod an open B-spline description given by

$$\boldsymbol{p}(\lambda) = \Sigma_{i=1}^{n} b_i^p(\lambda)\mathbf{P}_i \tag{54}$$

with $\lambda \in [0,1]$.

Similarly,

$$\phi(\lambda) = \Sigma_{i=1}^{n} b_i^p(\lambda)\phi_i \tag{55}$$

being ϕ_i the values of the correction angle at the control points.

Collecting the degrees of freedom in the vector $\boldsymbol{q}$ as follows

$$\mathbf{q} = \{\boldsymbol{P}_1, \phi_1, \boldsymbol{P}_2, \phi_2, ..., \boldsymbol{P}_n, \phi_n\} \tag{56}$$

the configuration of the rod is given by the interpolation

$$\{\boldsymbol{p}(\lambda), \phi(\lambda)\} = \mathbb{M}\mathbf{q} \tag{57}$$

with ($\boldsymbol{I}_4$ is the 4×4 identity matrix)

$$\mathbb{M} = \{\mathrm{diag}\mathbf{I}_4\, b_i^p\}. \tag{58}$$

As it is evident, in the single patch case the degrees of freedom are the displacements of the control point, and their torsional rotations. Rotations about the normal axes are not included in the model, and are calculated according to equations (30). From their construction, it can be seen that only the first two B-spline basis functions have non vanishing derivative at the first end (resp. only the last two at the second end), so that a boundary

condition on the rotation only affects the position of the first two control points. In particular, since the control polygon is tangent to the interpolated curve, the normal components of the velocity of the second and second last control points determine the velocity of the end bending rotations.

4.2. Geometric continuity for a curve

According to Barsky and DeRose[37] and Hohmeyer and Barsky[38] two curves meet with parametric continuity, C^1, if the parametric tangents, $\boldsymbol{t} = \frac{d\boldsymbol{p}}{d\lambda}$, are the same at the joint. Parametric continuity is dependent on the specific parametrization of the curve, thus the first derivative of the position vector is not an intrinsic property of an oriented curve.

Contrarily, two curves meet with geometric continuity, G^1, if their unit tangents are the same at the joint. The geometric continuity, as highlighted in Barsky and DeRose[37], is an intrinsic property, in the sense that it is independent under a generic re-parametrization of the curves.

In this work it is proposed a G^1 parametrization for a curve based on the concept of the end rotations, similar to the Hermitian interpolation for the Euler-Bernoulli beam model.

4.3. A G^1 multipatch interpolation of the centroid curve

Let's examine the simplest case of a single beam that we wish to divide in many patches. Concentrated loads may be applied at the joints. The general case of beams matching with different orientation at the joints can be treated in a similar way.

We assume that the initial positioning of the patches satisfy geometric G^1 continuity at the joints, that guarantees that the tangent vector $\hat{\boldsymbol{t}}_0$ is everywhere continuous. This can be obtained in several ways, and will not be discussed here.

The scheme discussed in the previous sections can not be applied directly to the case of a multipatch beam. Indeed, since, as has been observed, only the displacements are used as degrees of freedom, rotations around the normal axes at the joints are not constrained, so that a kinematically undetermined structure is obtained, leading to a singular stiffness matrix after assemblage. Additional constraints have to be enforced, specifically, the continuity of the rotations. The twist angle is interpolated by a continuous function, so that in order to guarantee the continuity of the rotations it is sufficient to enforce the continuity of the tangent vector direction. In this way a G^1 continuity is achieved. On the contrary, the norm of the tangent vector

is not constrained, since it is determined by the equilibrium equations, and may present a jump in the case a point force is applied at the node joining two patches.

In order to reach the required continuity the displacement degrees of freedom of the the second and second last control points are re-parametrized introducing the end rotations as degrees of freedom. A generalization of the Hermite interpolation to general open B-spline interpolation is so obtained, as will be described in detail.

A coordinate transformation is performed mapping the second, $\mathbf{P}_2$, and the second-last, $\mathbf{P}_{n-1}$, control points by means of the spatial rotations and the elongation of the end control segments tangent vectors $\tilde{\boldsymbol{t}}_{0,1}$ and $\tilde{\boldsymbol{t}}_{0,2}$ as follows (see fig. 2)

$$\mathbf{P}_2 = \mathbf{P}_1 + \rho_1 \tilde{\boldsymbol{R}}_1 \tilde{\boldsymbol{t}}_{0,1}, \quad \mathbf{P}_{n-1} = \mathbf{P}_n + \rho_2 \tilde{\boldsymbol{R}}_2 \tilde{\boldsymbol{t}}_{0,2}, \tag{59}$$

where $\tilde{\boldsymbol{R}}_1$ and $\tilde{\boldsymbol{R}}_2$ are the spatial rotation operators, the initial non unit tangent vectors are defined by the difference of the control points

$$\tilde{\boldsymbol{t}}_{0,1} = \mathbf{P}_{0,2} - \mathbf{P}_{0,1}, \quad \tilde{\boldsymbol{t}}_{0,2} = \mathbf{P}_{0,n-1} - \mathbf{P}_{0,n}, \tag{60}$$

and the scalars ρ_1 and ρ_2 are the relative changes in the lengths of these vectors, given by

$$\rho_1 = \frac{\|\mathbf{P}_2 - \mathbf{P}_1\|}{\|\mathbf{P}_{0,2} - \mathbf{P}_{0,1}\|} = \frac{\|\tilde{\boldsymbol{t}}_1\|}{\|\tilde{\boldsymbol{t}}_{0,1}\|}, \quad \rho_2 = \frac{\|\mathbf{P}_{n-1} - \mathbf{P}_n\|}{\|\mathbf{P}_{0,n-1} - \mathbf{P}_{0,n}\|} = \frac{\|\tilde{\boldsymbol{t}}_2\|}{\|\tilde{\boldsymbol{t}}_{0,2}\|}. \tag{61}$$

The configuration of the centroid curve is thus interpolated as

$$\begin{aligned} \boldsymbol{p}(\lambda) =& b_1^p(\lambda)\mathbf{P}_1 + \\ &+ b_2^p(\lambda)\left(\mathbf{P}_1 + \rho_1 \tilde{\boldsymbol{R}}_1 \tilde{\boldsymbol{t}}_{0,1}\right) + \\ &+ b_3^p(\lambda)\mathbf{P}_3 + ... + b_{n-2}^p(\lambda)\mathbf{P}_{n-2} + \\ &+ b_{n-1}^p(\lambda)\left(\mathbf{P}_n + \rho_2 \tilde{\boldsymbol{R}}_2 \tilde{\boldsymbol{t}}_{0,2}\right) + \\ &+ b_n^p(\lambda)\mathbf{P}_n. \end{aligned} \tag{62}$$

The G^1 parametric continuity is thus obtained equating the unit director $\hat{\tilde{\boldsymbol{t}}}_1^{k+1}$ at the first end of the $k+1$ patch with the unit director $\hat{\tilde{\boldsymbol{t}}}_2^{k}$ at the last end of the previous patch, i.e.

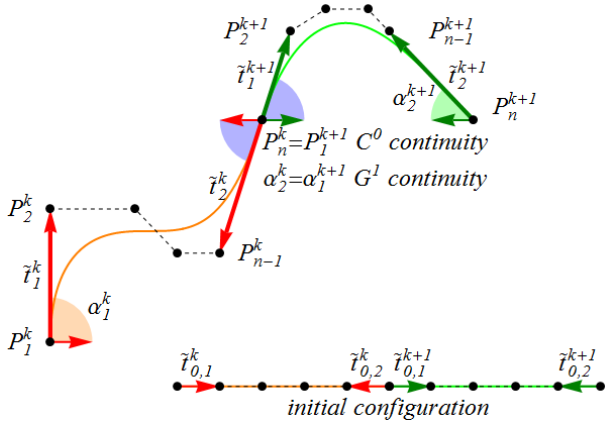

Figure 2: Geometric representation of the G^1 continuity as implicit constraint on the rotations at the joints of the elements.

$$\frac{\tilde{\boldsymbol{t}}_1^{k+1}}{\|\tilde{\boldsymbol{t}}_1^{k+1}\|} = -\frac{\tilde{\boldsymbol{t}}_2^{k}}{\|\tilde{\boldsymbol{t}}_2^{k}\|} \tag{63}$$

Recalling that $\hat{\tilde{\boldsymbol{t}}}_i^k = \tilde{\boldsymbol{R}}_i^k \hat{\boldsymbol{t}}_{0,i}^k$, equation (63) means that $\tilde{\boldsymbol{R}}_1^{k+1}\hat{\boldsymbol{t}}_{0,1}^{k+1} = -\tilde{\boldsymbol{R}}_2^k\hat{\boldsymbol{t}}_{0,2}^k$, and, since $\hat{\tilde{\boldsymbol{t}}}_{0,2}^k = -\hat{\tilde{\boldsymbol{t}}}_{0,1}^{k+1}$ the G^1 parametric continuity implies that $\tilde{\boldsymbol{R}}_1^{k+1} = \tilde{\boldsymbol{R}}_2^k$.

In terms of velocity equality (63) leads to

$$\dot{\hat{\tilde{\boldsymbol{t}}}}_2^k = -\dot{\hat{\tilde{\boldsymbol{t}}}}_1^{k+1} \tag{64}$$

and, observing that $\dot{\hat{\tilde{\boldsymbol{t}}}}_i^k = \dot{\tilde{\boldsymbol{R}}}_i^k\hat{\tilde{\boldsymbol{t}}}_{0,i}^k = \left(\dot{\tilde{\boldsymbol{R}}}_i^k\tilde{\boldsymbol{R}}_i^{k^{-1}}\right)\tilde{\boldsymbol{R}}_i^k\hat{\tilde{\boldsymbol{t}}}_{0,i}^k = \dot{\boldsymbol{\omega}}_i^k \times \hat{\tilde{\boldsymbol{t}}}_i^k$, we obtain that

$$\boldsymbol{\omega}_1^{k+1} \times \hat{\tilde{\boldsymbol{t}}}_1^{k+1} = -\boldsymbol{\omega}_2^k \times \hat{\tilde{\boldsymbol{t}}}_2^k \tag{65}$$

Therefore, the G^1 continuity requirement is satisfied if the velocities $\boldsymbol{\omega}_i$ are the same at adjacent patch ends.

Accounting for the new parametrization given by equation (59), and for the result

$$\dot{\tilde{\boldsymbol{t}}}_i^k = \dot{\rho}_i^k\frac{\tilde{\boldsymbol{t}}_i^k}{\rho_i^k} + \boldsymbol{\omega}_i^k \times \tilde{\boldsymbol{t}}_i^k \tag{66}$$

the velocity of the centroid curve is given by

$$
\begin{aligned}
\dot{\boldsymbol{p}}(\lambda) = &\left(b_1^p(\lambda) + b_2^p(\lambda)\right)\dot{\mathbf{P}}_1 + \\
&+ b_2^p(\lambda)\left(\dot{\rho}_1\,\frac{\tilde{\boldsymbol{t}}_1}{\rho_1} - \tilde{\boldsymbol{t}}_1 \times \boldsymbol{\omega}_1\right) \\
&+ b_3^p(\lambda)\dot{\mathbf{P}}_3 + ... + b_{n-2}^p(\lambda)\dot{\mathbf{P}}_{n-2} + \\
&+ b_{n-1}^p(\lambda)\left(\dot{\rho}_2\,\frac{\tilde{\boldsymbol{t}}_2}{\rho_2} - \tilde{\boldsymbol{t}}_2 \times \boldsymbol{\omega}_2\right) \\
&+ \left(b_n^p(\lambda) + b_{n-1}^p\right)\dot{\mathbf{P}}_n.
\end{aligned}
\tag{67}
$$

The velocity of the torsional angle is given by

$$
\dot{\phi}(\lambda) = \Sigma_{i=1}^{n} b_i^p(\lambda)\dot{\phi}_i \tag{68}
$$

In (68) the first and the last values must be represented in terms of the end rotation vectors as $\dot{\phi} = \boldsymbol{\omega} \cdot \hat{\boldsymbol{t}}$ so that, observing that $\hat{\boldsymbol{t}}|_0 = \hat{\tilde{\boldsymbol{t}}}_1, \hat{\boldsymbol{t}}|_L = -\hat{\tilde{\boldsymbol{t}}}_2$, the interpolation of the velocity of rotation around the centroid curve, is

$$
\begin{aligned}
\dot{\phi}(\lambda) = &b_1^p(\lambda)\,\boldsymbol{\omega}_1 \cdot \hat{\tilde{\boldsymbol{t}}}_1 + \\
&+ b_1^p(\lambda)\dot{\phi}_2 ... + b_{n-1}^p(\lambda)\dot{\phi}_{n-1} \\
&+ b_n^p(\lambda)\,\boldsymbol{\omega}_2 \cdot (-\hat{\tilde{\boldsymbol{t}}}_2).
\end{aligned}
\tag{69}
$$

The newly defined degrees of freedom of the velocities are collected in the vector $\dot{\boldsymbol{y}}$ defined as

$$
\dot{\boldsymbol{y}} = \{\dot{\mathbf{P}}_1, \boldsymbol{\omega}_1, \dot{\rho}_1, \dot{\phi}_2; \dot{\mathbf{P}}_3, \dot{\phi}_3, ..., \dot{\mathbf{P}}_{n-2}, \dot{\phi}_{n-2}; \dot{\phi}_{n-1}, \dot{\rho}_2, \dot{\mathbf{P}}_n, \boldsymbol{\omega}_2\} \tag{70}
$$

The coordinates $\boldsymbol{y}$ and $\boldsymbol{q}$ are related through a linear transformation, that actually involves only the first two and the last two control points. With the notation $\mathbf{0}_3 = \{0, 0, 0\}$ it is:

$$\dot{\boldsymbol{q}}_{1,2} = \mathbb{E}_1 \dot{\boldsymbol{y}}_{1,2}, \qquad \dot{\boldsymbol{q}}_{n-1,n} = \mathbb{E}_2 \dot{\boldsymbol{y}}_{n-1,n}$$

$$\mathbb{E}_1 = - \begin{pmatrix} \boldsymbol{I}_3 & \boldsymbol{0}_3 & 0 & 0 \\ \boldsymbol{0}_3^T & \hat{\tilde{\boldsymbol{t}}}_1 \cdot & 0 & 0 \\ \boldsymbol{I}_3 & -\tilde{\boldsymbol{t}}_1 \times & \frac{\tilde{\boldsymbol{t}}_1}{\rho_1} & 0 \\ \boldsymbol{0}_3^T & \boldsymbol{0}_3^T & 0 & 1 \end{pmatrix}, \tag{71}$$

$$\mathbb{E}_2 = - \begin{pmatrix} \boldsymbol{0}_3^T & \frac{\tilde{\boldsymbol{t}}_2}{\rho_2} & \boldsymbol{I}_3 & -\tilde{\boldsymbol{t}}_2 \times \\ 1 & 0 & \boldsymbol{0}_3 & \boldsymbol{0}_3 \\ \boldsymbol{0}_3^T & \boldsymbol{0}_3^T & \boldsymbol{I}_3 & \boldsymbol{0}_3 \\ 0 & 0 & \boldsymbol{0}_3 & \hat{\tilde{\boldsymbol{t}}}_2 \cdot \end{pmatrix}.$$

Figures 3(a) and 3(b) show the interpolation functions for the velocities in the case of Bernstein's polynomials of degree 3. In this case the proposed transformation yields exactly the Hermite shape functions. Figures 3(c) and 3(d) are related to Bernstein's polynomials of degree 4 and corresponding transformed G^1-functions; Figures 3(e) and 3(f) are related to a B-spline of degree 3 with internal knots and corresponding transformed G^1-B-spline. As observed previously, only the first and last two interpolation functions are modified.

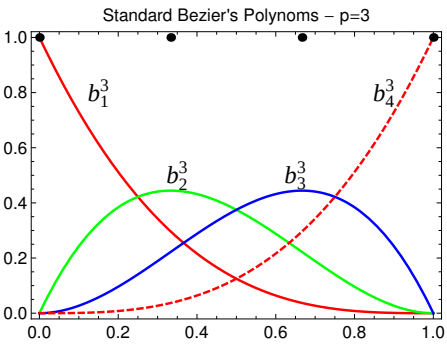

(a) C^0 Bernstein interpolation functions (polynomial degree p=3).

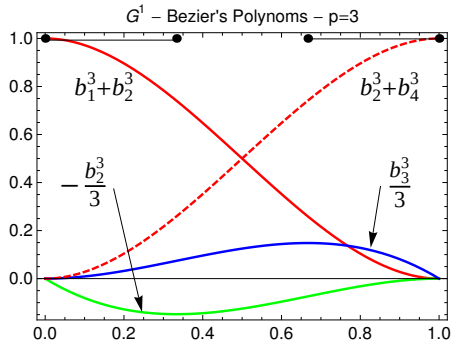

(b) G^1 Bernstein interpolation functions (Hermitian f. p=3).

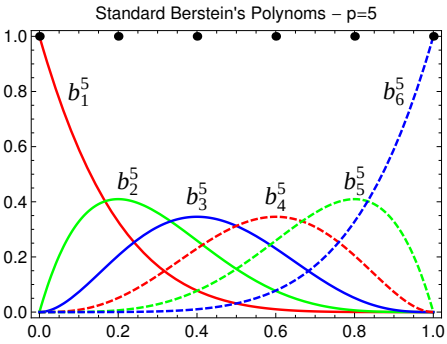

(c) C^0 Bernstein interpolation functions (polynomial degree p=5).

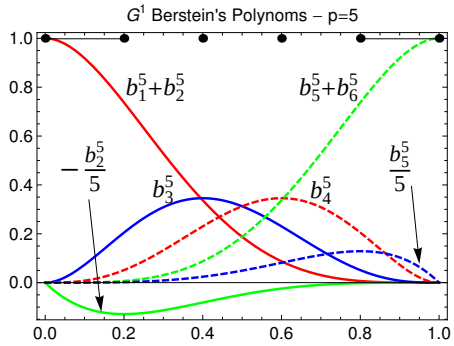

(d) G^1 Bernstein interpolation functions (polynomial degree p=5).

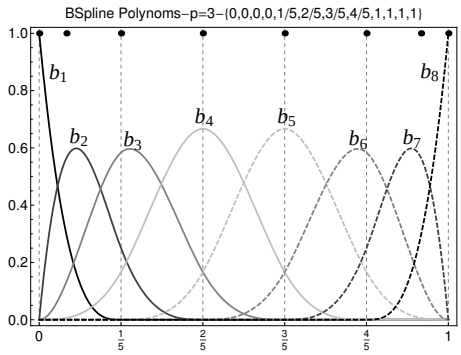

(e) Standard C^0 B-spline interpolation (polynomial degree p=3).

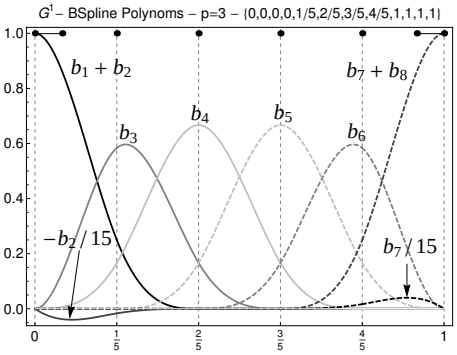

(f) G^1 B-spline interpolation (polynomial degree p=3).

Figure 3: Transformation of shape function from standard C^0 open B-spline to G^1 open B-spline shape functions, (with or without internal knots).

5. Numerical results

In this section the performance of the proposed G^1-multi-patch method with low inter element continuity is compared with the B-spline approach with high inter-element continuity. In both cases the Kirchhoff-Love model is used, adopting the same quadrature rule, namely a Gauss-Lobatto integration with $p+1$ points for each element. Refinement is obtained using an $h-$refinement scheme for the B-spline approach, that leaves the inter element continuity invariant, while for the G^1 multi patch approach refinemebt is obtaoned increasing the number of patches.

First are presented simple academic examples aimed to analyze the influence of the continuity degree on the accuracy and on the rate of convergence of the solution. The measure adopted for the error is the L^2 error norm defined as

$$e_{L^2}(\bullet) = \frac{\|(\bullet)_p - (\bullet)_{exact}\|}{\|(\bullet)_{exact}\|} \tag{72}$$

Four examples are presented. The first is a plane arch, where only bending and axial deformations are present. Then an horizontal arch with bending-torsional coupling is examined. The third example is similar to the second, but an initial pre-twist of the arch has been considered, in order to evaluate the influence of pre-twisting on the results. The fourth example concerns an arch with discontinuity on the stresses.

Subsequently, it is considered the case of 3D assembly of Kirchhoff Love rods, in which the elements are curved and pre-twisted; These analyses are performed with G^1 multi patch elements only.

In all the cases examined linear elastic behavior and small deformations are considered.

5.1. 2D cantilever arch with a point force at the free end

In this example it is considered a 2D cantilever circular arch loaded at the tip by a vertical force $\boldsymbol{F} = \{0, -1, 0\}, [kN]$. The radius of the centroid curve is $R = 1\,[m]$ the section is rectangular with $h_n = 0.1$ and $h_\nu = 0.01\,[m]$ respectively, $\hat{\boldsymbol{n}}(S) = \boldsymbol{e}_z$, $\hat{\boldsymbol{\nu}} = \hat{\boldsymbol{t}} \times \boldsymbol{e}_z$ and $E = 2.0 * 10^8\,[kN/m^2]$. See figure 4 for the geometry.

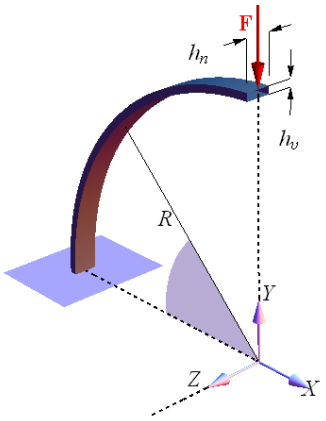

Figure 4: 2D cantilever arch with a point force at the free end.

The rate of convergence of the G^1 formulation is examined for three different polynomial degrees $p = 3, 4, 5$ in the plots of figures 5. On the horizontal axis is reported the number of control points used in the approximation, proportional to the number of degrees of freedom. In the graphs, dotted lines show the rate of convergence, and a number next to them indicates its value. The error is evaluated according to formula (72) using as reference solution the analytical one, reported in **??**.

Figure 5(a) presents the L^2 norm of the error for the displacement component $u_y(S)$, obtained with the multi-patch approach for the three polynomial degrees adopted. The asymptotic rate of convergence for the displacement error is in any case higher than the theoretical value $p + 1$.

In figures 5(b),5(c),5(d) the error obtained with the multi-patch and the single patch B-spline approaches are separately compared for each one of the three polynomial degrees used. The same rate of convergence is obtained for both the (high continuity level) B-spline and for the (low continuity level) G^1 multi patch approaches; However, the accuracy obtained with the single

patch approximation is higher that the accuracy obtained with the multi-patch approach.

Figure 6 shows the rate of convergence of the error for the effective axial force and bending moment, separately reporting the error for the multipatch approach (figures 6(a), 6(c)) and for the single patch approach (figures 6(b), 6(d)). Contrary to what was found for the displacement errors, in this case the asymptotic rate of convergence matches the theoretical values, respectively p and $p-1$ for the axial and the bending stress resultants. The same asymptotic rate of convergence is found for single patch and multi-patch approaches but the accuracy obtained with the (high continuity) B-spline approach is higher than that obtained with the (low continuity) G^1-multi-patch approach, in agreement with what was observed in Echter and Bischoff[39]. Furthermore, as appears from figures 6(a) and 6(c), the accuracy obtained for the bending moment is higher than the accuracy obtained for the axial force.

The case of a multi-patch dicretization using cubic B-splines with internal knots in each patch is considered in figure 7, where is plotted the error on the vertical displacement obtained using the multi-patch approach with Bezier interpolation and with B-spline interpolations with 1,2 and 3 internal knots, and the errors obtained using the single patch B-spline approach. The first and the last curves are the same as in figures 5(b). The errors are plotted versus the number of control points used in the interpolation. Adding internal knots does not modify the rate of convergence of the error, but improves the accuracy, that tends toward the accuracy obtained with the single patch B-spline interpolation.

Figure 8 shows the influence of the thickness ratio h_ν/R on the L^2 error for the displacements using different discretizations. The results presented have been obtained with cubic B-splines. Figure 8(a) reports the error for the G^1 multi-patch case, employing from 1 up to 10 patches, while figure 8(b) refer to the single patch approach using an increasing number of blended elements. The numbers written next to the curves indicate the number of control points introduced by the discretization. The results relative to the single patch interpolation (figure 8(b)) show a high sensitivity of the error to the thickness ratio h_ν/R. As the ratio gets smaller and smaller, the error increases, tending to 100%, no matter what the discretization is. This behaviour is due to the presence of membrane locking, as usually observed in standard FEM applications.

Also in the multi-patch case the accuracy of the solution decreases with

increasing slenderness of the rod, indicating that also in this case some membrane locking is still present. However the dependency of the accuracy on the thickness ratio is much smaller than for the single-patch approach. Furthermore, even for very small thickness ratios the error decreases as the discretization improves, differently from what happens with the single patch solution.

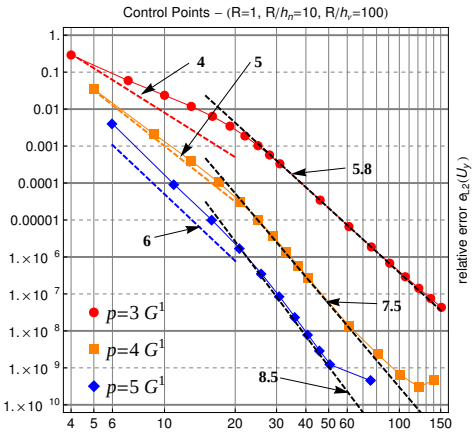

(a) L^2 error norm of u_y for the G^1-multi-patch approach, with different polynomial degrees.

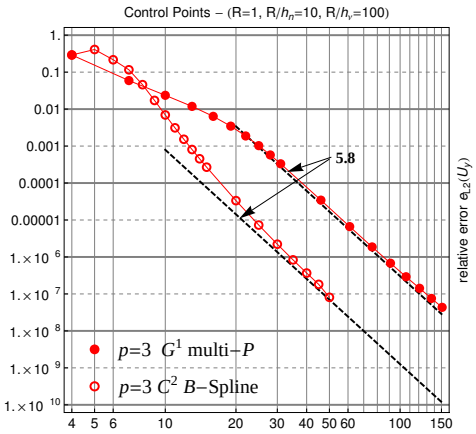

(b) L^2 error norm of u_y for $p = 3$. Comparison between single patch and G^1-multi-patch approach.

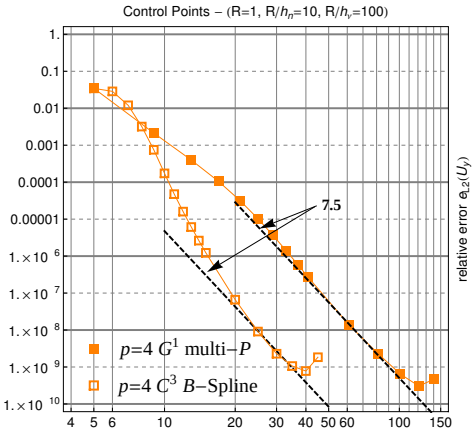

(c) L^2 error norm of u_y for $p = 4$. Comparison between single patch and G^1-multi-patch approach.

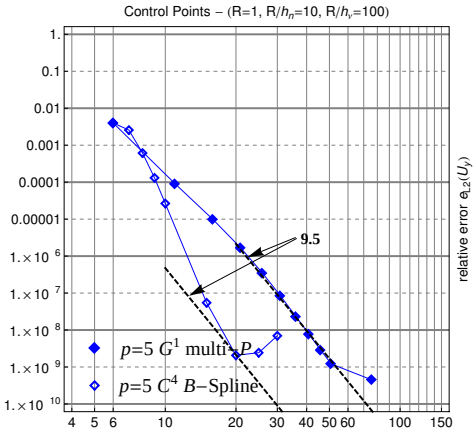

(d) L^2 error norm of u_y for $p = 5$. Comparison between single patch and G^1-multi-patch approach.

Figure 5: Relative error in L^2 norm for the u_y displacement component, $e_{L^2}(u_y)$, versus the number of control points for $\frac{R}{h_\nu} = 100$.

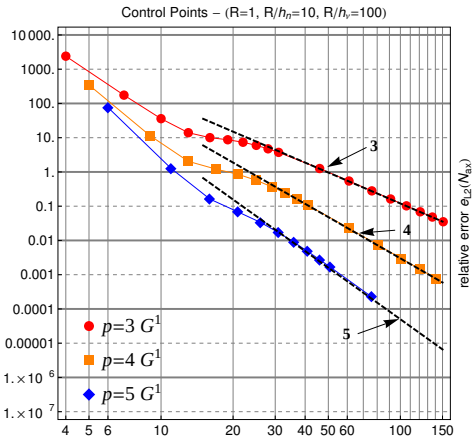

(a) L^2 error norm of N_{eff} for the G^1-multi-patch approach, with different polynomial degrees.

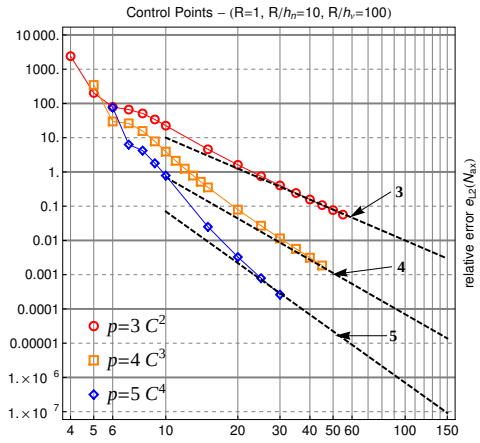

(b) L^2 error norm of N_{eff} for B-spline standard k-refinement, with different polynomial degrees.

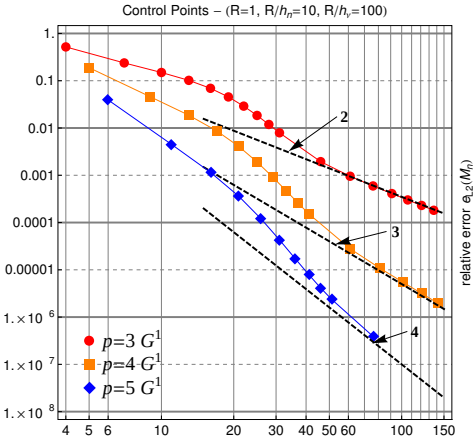

(c) L^2 error norm of M_n for the G^1-multi-patch approach, with different polynomial degrees.

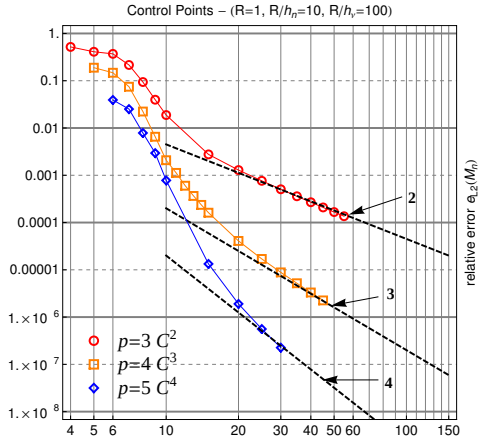

(d) L^2 error norm of M_n for B-spline standard k-refinement, with different polynomial degrees.

Figure 6: Relative errors in L^2 norm for the axial force and bending moment, versus the number of control points with $\frac{R}{h_\nu} = 100$.

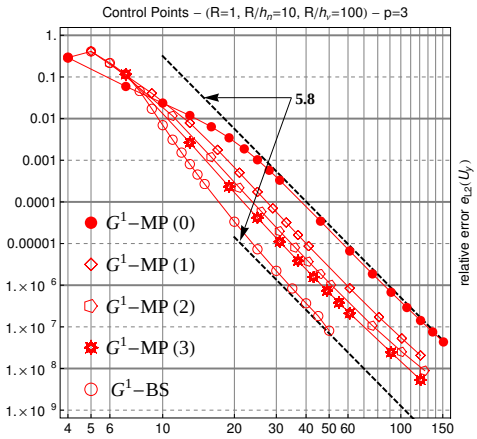

Figure 7: Relative error in L^2 norm for the displacement component u_y. Transition from uniform B-spline to G^1 Multi-patch solution using k-refinement in the different patches.

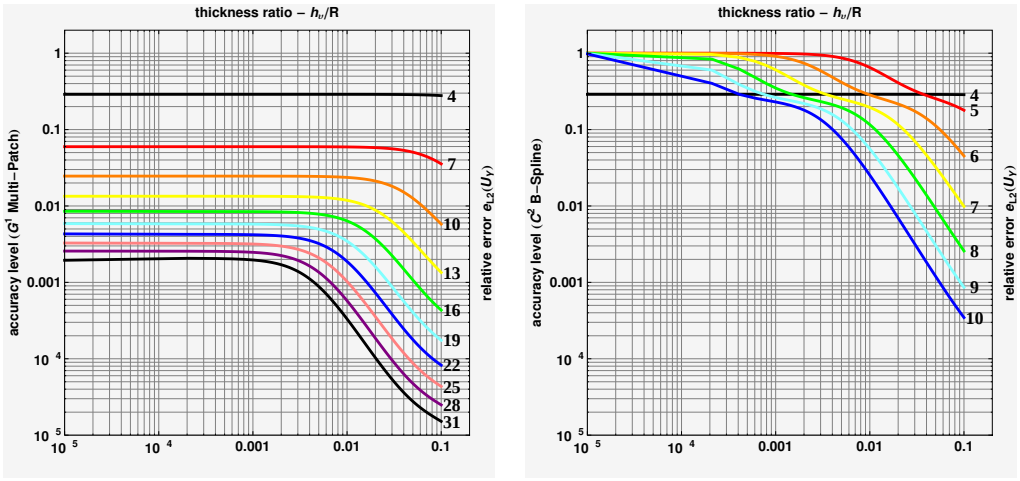

(a) L^2 error norm of the displacement u_y for the G^1-multi-patch approach.

(b) L^2 error norm of the displacement u_y for the single patch approach.

Figure 8: Influence of the thickness ratio h_ν/R on the error in L^2 norm of the displacement u_y for different discretizations, for the polynomial degree $p = 3$.

5.2. Horizontal 3D cantilever arch with a point force at the free end

In this example it is considered a horizontal 3D cantilever circular arch loaded at the tip by a vertical force $\boldsymbol{F} = \{0, 0, -1\}, [kN]$. Bending and torsion are coupled in this example. The radius of the centroid curve is $R = 1\,[m]$ the section is rectangular with $h_n = 0.1$ and $h_\nu = 0.01\,[m]$ respectively, $\hat{\boldsymbol{n}}(S) = \boldsymbol{e}_z$, $\hat{\boldsymbol{\nu}} = \hat{\boldsymbol{t}} \times \boldsymbol{e}_z$ and $E = 2.0 * 10^8\,[kN/m^2]$; for the geometry see figure 9. The same analyses as in the previous example are presented.

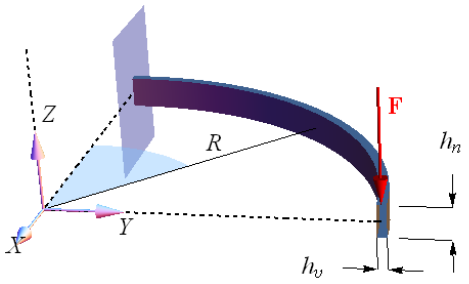

Figure 9: Geometry of the 3D cantilever arch with a point force at the free end.

Figure 10 shows the rate of convergence of the errors in L^2 norm for the torsional angle ϕ. The G^1-multi-patch approach is presented in figure 10(a), the single patch approach in figure 10(b). The polynomial degrees $p = 3, 4, 5$ have been investigated. The asymptotic rate of convergence for the L^2 error of the torsional angle ϕ coincides with the theoretical limit, $p + 1$ and also for this case the same asymptotic rate has been obtained for the single patch and the G^1-multi-patch analyses. The accuracy obtained with single patch approach is higher than the accuracy obtained with the multi-patch approach.

The errors obtained for the bending and torsional moments are presented in figures 11 and 12. The asymptotic rate of convergence equals the theoretical rate $p - 1$ and p, respectively, conformingly to the previous example. Comparing the errors with those found with the single patch approach the same asymptotic rate of convergence is obtained, but the accuracy of the latter solutions is better (figures 11(b), 12(b). Only in the case $p = 3$ the convergence rate for the error on the torsional moment for the single patch interpolation reduces to the value $p = 2$, as appears from figure 12(b), related to the torsional moment. This phenomenon is due to the presence of locking.

Figure 13 presents the dependency of the error for the torsional angle ϕ on the thickness ratio in the case $p = 3$, comparing the results for the multi-patch

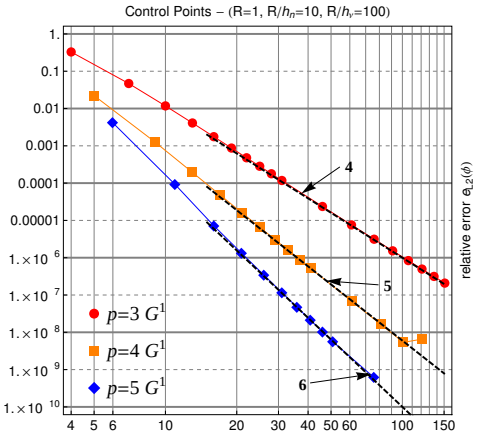

(a) L^2 error norm of ϕ for the G^1-multi-patch approach, with different polynomial degrees.

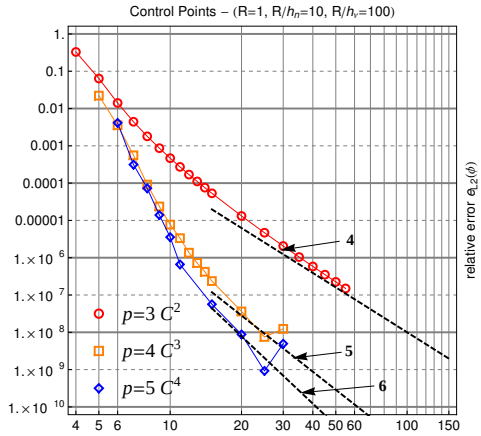

(b) L^2 error norm of ϕ for B-spline standard k-refinement, with different polynomial degrees.

Figure 10: Relative error in L^2 norm for the torsional angle ϕ versus the number of control points with $\frac{R}{h_\nu} = 100$.

(figure 13(a)) and for the single-patch B-spline interpolations (figure 13(b)). Similarly to what was found in the previous example, flexural locking clearly occurs in the solution, as can be observed from the dependency of the error on the thickness ratio. However, also in this case locking is much less severe for the multi-patch discretization than for the single patch discretization, indicating that relaxing the continuity of the solution helps in reducing the phenomenon.

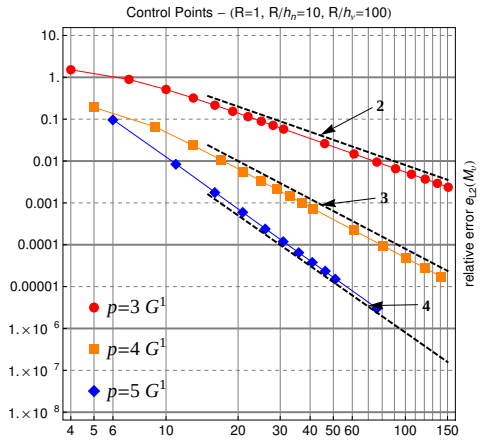

(a) L^2 error norm of M_ν for the G^1-multi-patch approach, with different polynomial degrees.

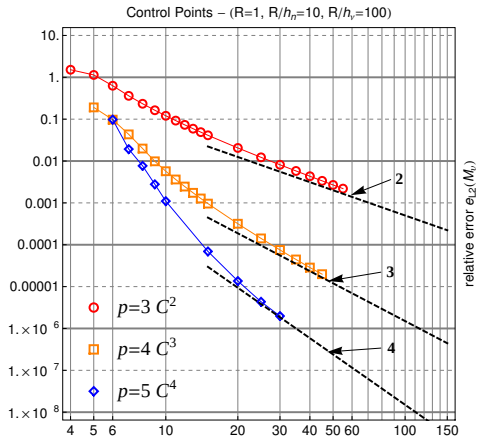

(b) L^2 error norm of M_ν for B-spline standard k-refinement, with different polynomial degrees.

Figure 11: Relative error in L^2 norm for the bending moment versus the number of control points with $\frac{R}{h_\nu} = 100$.

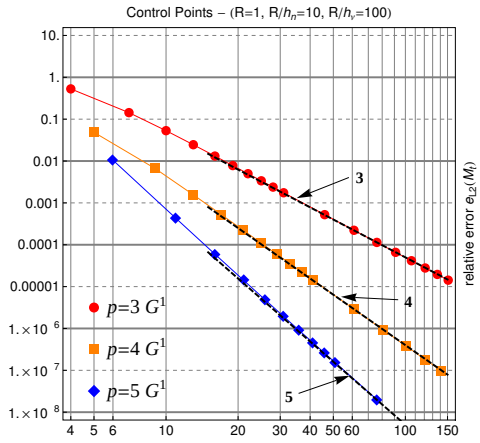

(a) L^2 error norm of M_t for the G^1-multi-patch approach, with different polynomial degrees.

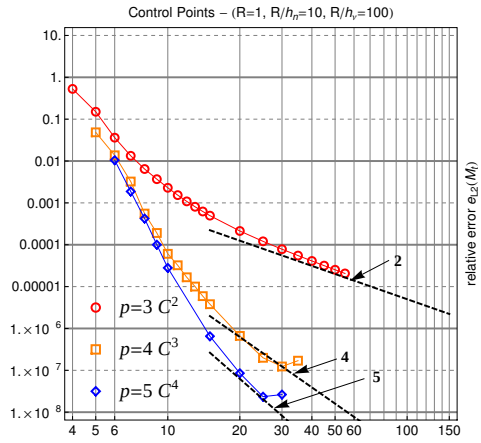

(b) L^2 error norm of M_t for B-spline standard k-refinement, with different polynomial degrees.

Figure 12: Relative error in L^2 norm for the twisting moment versus the number of control points with $\frac{R}{h_\nu} = 100$.

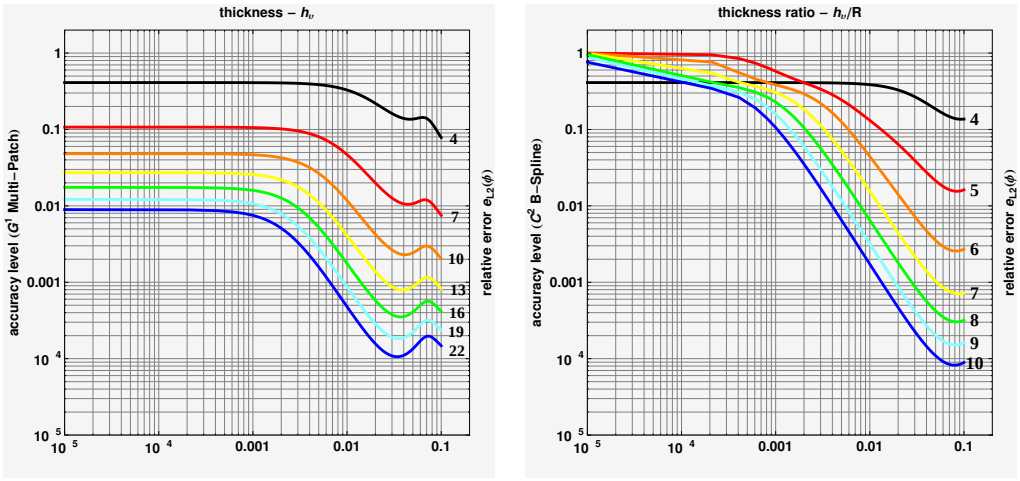

(a) L^2 error norm of the rotation ϕ for the G^1-multi-patch approach.

(b) L^2 error norm of the rotation ϕ for the single patch approach.

Figure 13: Influence of the thickness ratio h_ν/R on the error in L^2 norm of the torsion angle ϕ for different discretizations, for the polynomial degree $p = 3$.

5.3. 3D pre-twisted cantilever arch with a point force at the free end

In this section it is considered the same arch of the previous example but with an initial twist. The unit normal is given by $\hat{\boldsymbol{n}}(S) = \boldsymbol{R}(\phi_0(S), \hat{\boldsymbol{t}}(S))$, where $\phi_0(S) = S$, with $S \in [0, \frac{\pi}{2}]$. In figure 14 the considered geometry is shown .

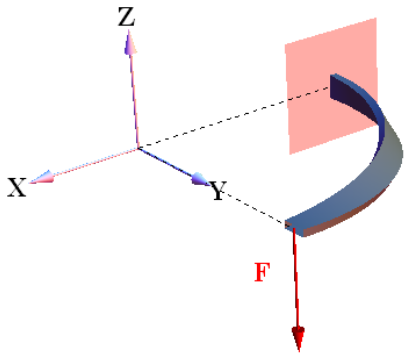

Figure 14: 3D pre-twisted cantilever arch with shear at the free end.

The error for the vertical displacement u_z is examined in figure 15. Also in this case, that presents full bending and torsional coupling, the rate of convergence is higher than the theoretical limit $p+1$ for all the polynomial degrees considered ($p = 3, 4, 5$), both for the G^1 and for the single-patch approach. The same results have been obtained for the horizontal components of the displacement, u_x and u_y, not reported for brevity. The rate of convergence of the correction angle ϕ is instead close to the theoretical rate.

The errors for the bending and torsional components of the internal moment are presented in figures 16, 17. As was found in the previous example, the asymptotic rates of convergence are $p-1$ and p respectively, no matter what kind of interpolation is used, and also for this highly coupled example the single-patch approach with high continuity is more accurate than the multi-patch approach with reduced continuity, except for the torsional moment in the case $p = 3$.

Analysing the influence of the thickness ratio on the solution shows that also in this case the accuracy is influenced by the thickness ratio, suggesting that bending-torsional locking is present. Also in this case the G^1 multi-patch interpolation behaves better than the single patch interpolation.

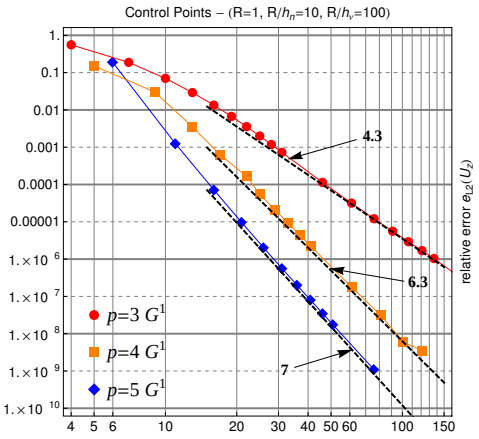

(a) L^2 error norm of u_z for the G^1-multi-patch approach, with different polynomial degrees.

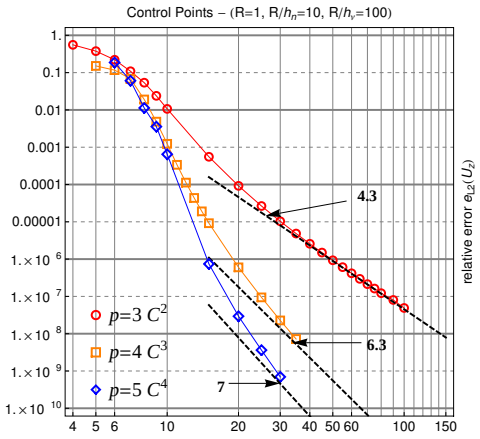

(b) L^2 error norm of u_z for B-spline standard k-refinement, with different polynomial degrees.

Figure 15: Relative error in L^2 norm for the displacement component u_z versus the number of control points with $\frac{R}{h_\nu} = 100$.

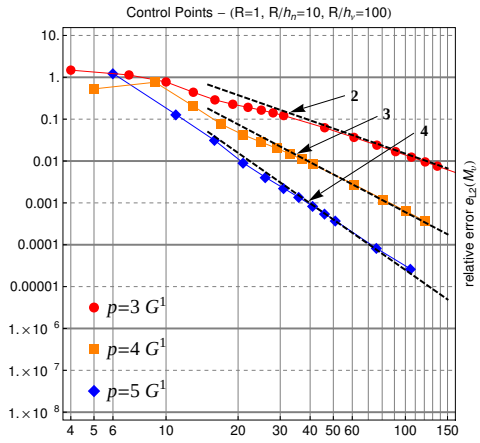

(a) L^2 error norm of M_ν for the G^1-multi-patch approach, with different polynomial degrees.

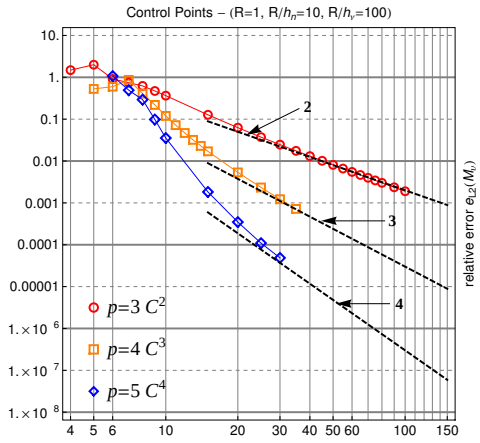

(b) L^2 error norm of M_ν for B-spline standard k-refinement, with different polynomial degrees.

Figure 16: Relative error in L^2 norm for the bending moment, versus the number of control points with $\frac{R}{h_\nu} = 100$.

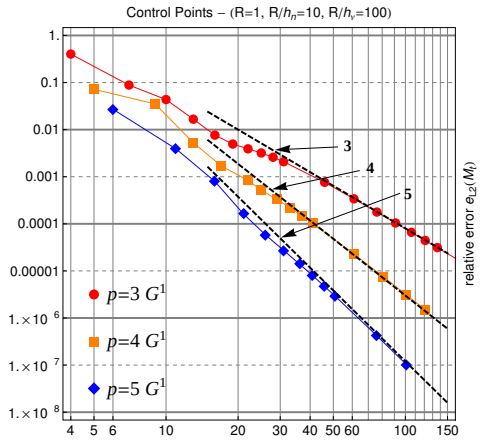

(a) L^2 error norm of M_t for the G^1-multi-patch approach, with different polynomial degrees.

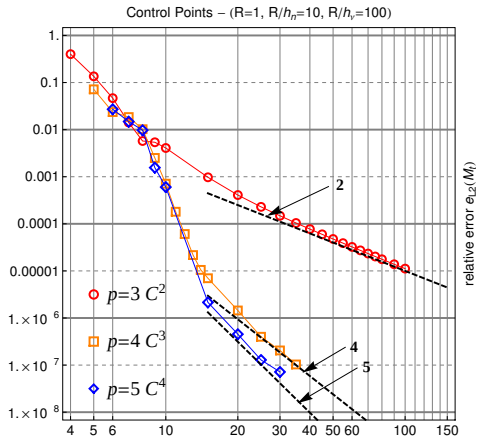

(b) L^2 error norm of M_t for B-spline standard k-refinement, with different polynomial degrees.

Figure 17: Relative error in L^2 norm for the twisting moment M_t versus the number of control points with $\frac{R}{h_\nu} = 100$.

5.4. A 2D arch with a point force along the span.

In this section it is considered a 2D plane circular arch loaded by a point force at the mid arch span. Figure 18(a) shows the geometry and the load considered. The vertical force has an intensity of $1[kN]$. The radius of the centroid curve is $R = 1\,[m]$ the section is rectangular with $h_n = 0.01$ and $h_\nu = 0.1\,[m]$ respectively, $\hat{\boldsymbol{n}}_{\mathbf{0}}(0) = \boldsymbol{e}_x$, $\hat{\boldsymbol{\nu}} = \hat{\boldsymbol{t}} \times \boldsymbol{e}_z$ and $E = 2.0 * 10^8\,[kN/m^2]$. The problem is modeled with quintic polynomials. When a single patch is used, at the loaded node a C^4 internal continuity is present. The error is evaluated with respect to the exact solution calculated using the Green function reported in Cuomo and Ventura [40].

A convergence analysis of the solution is presented in figures 18(b) and 18(c), in which are plotted the L^2-error for the stress resultants obtained with the two approximations. Figure 18(b) refers to the error for the effective axial force N_{eff}, and figure 18(c) to the error for the bending moment M_n. In both cases, for this example, the error measured on the single patch solution is larger than the error obtained with the multi patch approach. Especially for the axial force the single patch solution shows a very slow convergence rate. The rate of convergence of the multi patch solution, on the contrary, is close to the theoretical rate, as was found in the other applications.

The reasons of this behaviour can be understood from the plots of the bending moment and of the axial force, reported in figure 19, for the two strategies considered. The comparison is performed with the same number of control points. (In the multi patch model 8 patches are considered equivalent to 41 control points, while in the case of the single patch model 36 (non null) sections are considered, that correspond to the same number of control points). Significative errors appear in the axial force distribution in the single patch case (figure 19(d)), due to the high internal continuity that prevents from accurately detect the jump in the value of the axial force.

The G^1 solution is far more accurate, thanks to the fact that different stretch ratios ρ were introduced as degree of freedom at the joints of the patches.

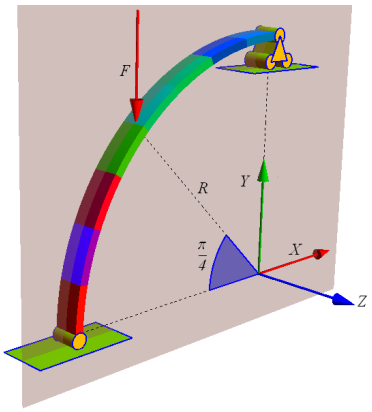

(a) Geometry and constraints of the 2D circular arch.

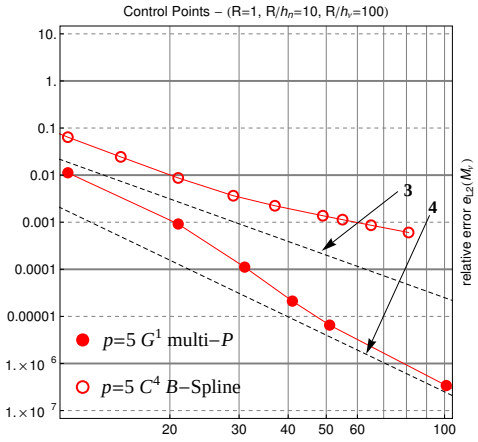

(b) L^2 error norm for the bending moment M_ν for single patch and multi-patch approaches, with $p = 5$.

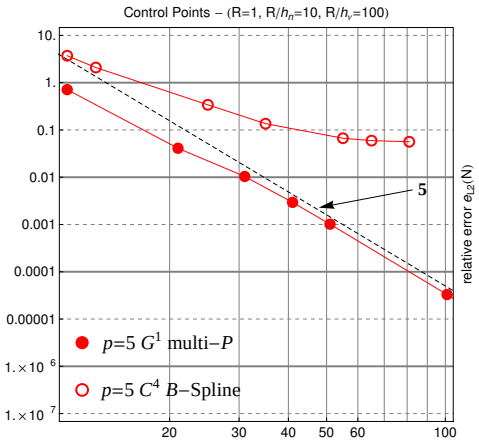

(c) L^2 error norm for the axial force N_{eff} for single patch and multi-patch approaches, with $p = 5$.

Figure 18: Problem's geometry and convergence analyzes for the error in L^2 norm of stress resultants.

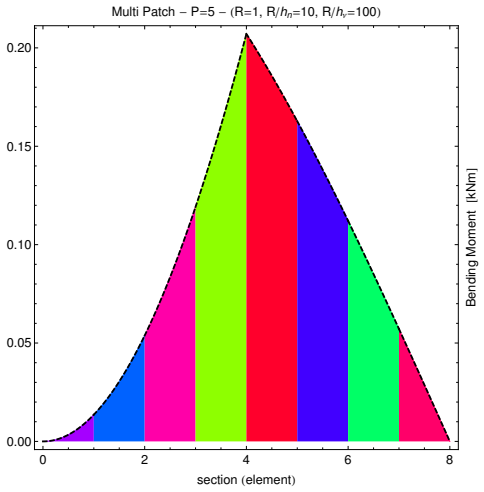

(a) Bending moment M_ν: exact (dashed) and multi patch solution.

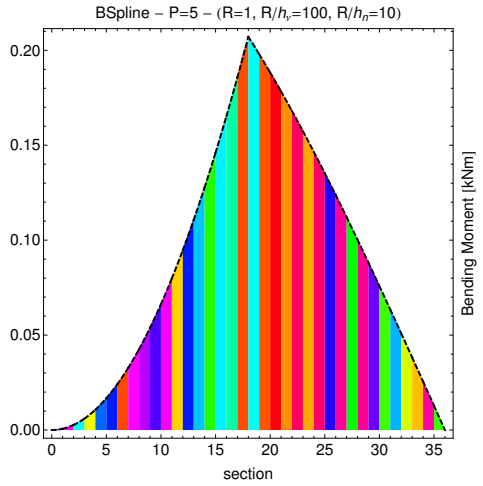

(b) Bending moment M_ν: exact (dashed) and single patch solution.

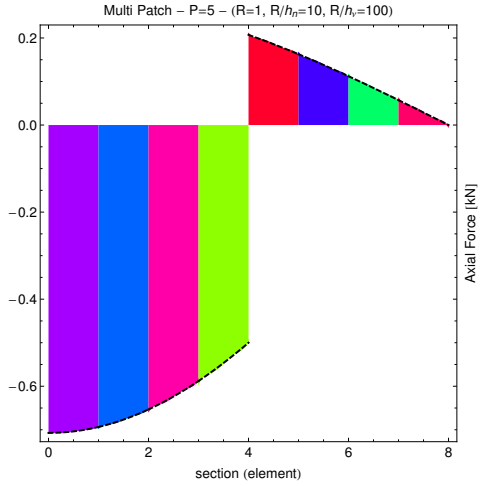

(c) Axial force N_{eff}: exact (dashed) and multi patch solution.

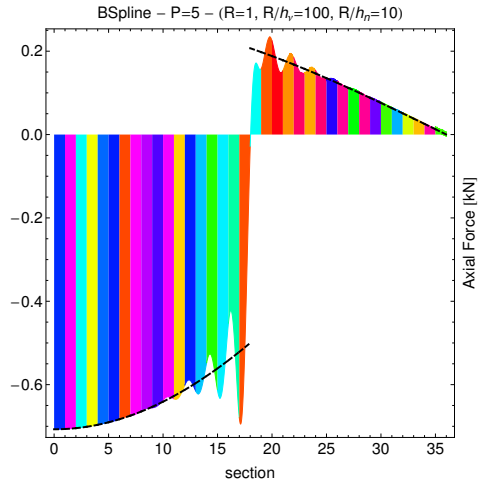

(d) Axial force N_{eff}: exact (dashed) and single patch solution.

Figure 19: Comparison for the stress resultants obtained with the two strategies, for the same number of degrees of freedom.

5.5. Grid assemblies of Kirchhoff-Love rods

As conclusive examples, some structures of engineering interest are presented. The two grids represented in figure 20 have been analyzed. The first realizes an hypar surface by means of pre-twisted rods; the second is a grid used for sustaining a cylindrical light roof, and in this case the rods are curved and pre-twisted. These structures are commonly made out of laminated timber elements, that are twisted prior to gluing. The grids have been modeled by Kirchhoff-Love rods lying along a double family of curves generated on the surface. The normal $\hat{\boldsymbol{n}}$ to each rod has been taken coincident with the normal to the surface, in this manner the initial rod geometry is affected by bending curvatures and torsion. The use of the proposed parametrization related to the multi-patch approach allows to simply model the complex geometry of the structure, avoiding the introduction of additional kinematic constraints.

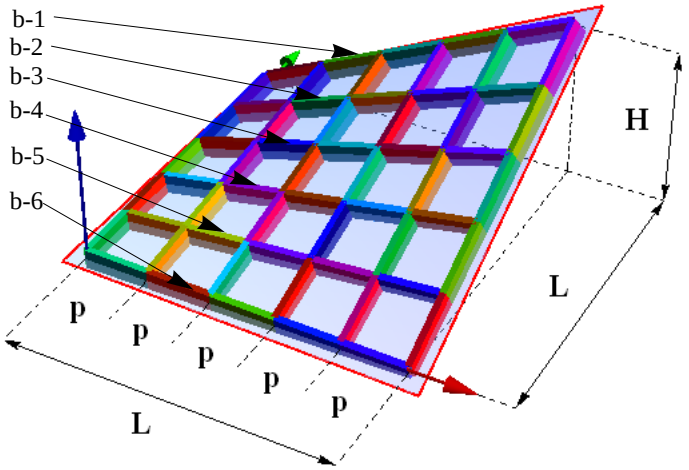

(a) Hypar surface.

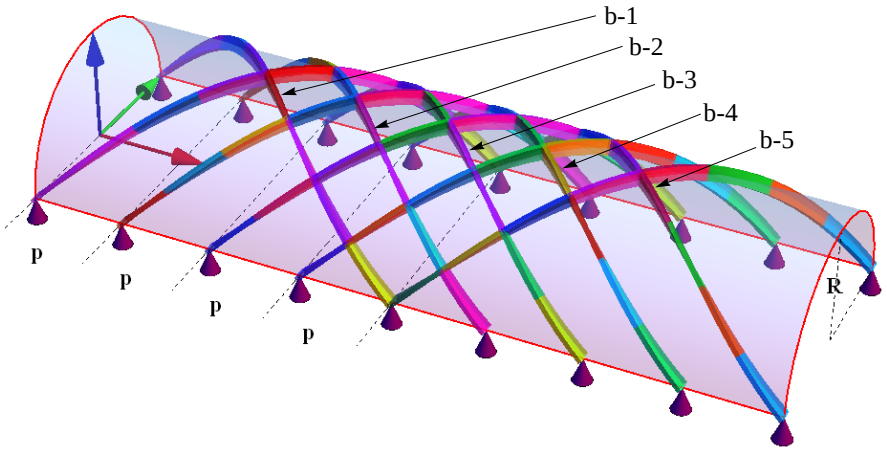

(b) Cylindrical surface.

Figure 20: Geometry of the grids considered in section 5.5.

5.5.1. The hyperboloid grid

The hyperboloid is a lined surface, defined by two families of non geodetic lines. All the vertices have a quota $z = 0\,[m]$ except one highest vertex that has a quota $H = 2.5\,[m]$. The data used were $L = 5\,[m]$ and $p = 1\,[m]$, see figure 20(a). The three corner points at the same quota are fixed, while on the highest point is applied a unit vertical force $\boldsymbol{F} = \{0, 0, -1\}\,[kN]$, represented in figure 21. Quintic G^1 multi-patch elements are used for the interpolation. All the rods have rectangular cross section with $h_n = 0.4\,[m]$ and $h_\nu = 0.2\,[m]$, and the material has Young's modulus $E = 1 * 10^7\,[kN/m^2]$ and shear modulus $G = 5 * 10^5\,[kN/m^2]$. A magnified sketch of the deformed configuration under the action of the considered load is shown in Figure 21. The evaluated displacement of the loaded corner is $\boldsymbol{u}_F = \{0.000695642, 0.000695642, -0.00142854\}\,[m]$. The bending moment M_ν for the five beams of the element group $b - 6$ is represented in figure 22. The different elements are indicated with different colors. The moment is not continuous at the joints, as expected.

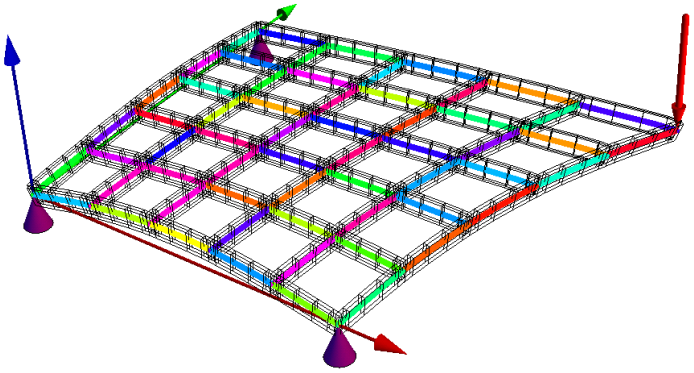

Figure 21: Initial and Magnified (MF=2000) deformed configurations for the hypar-grid.

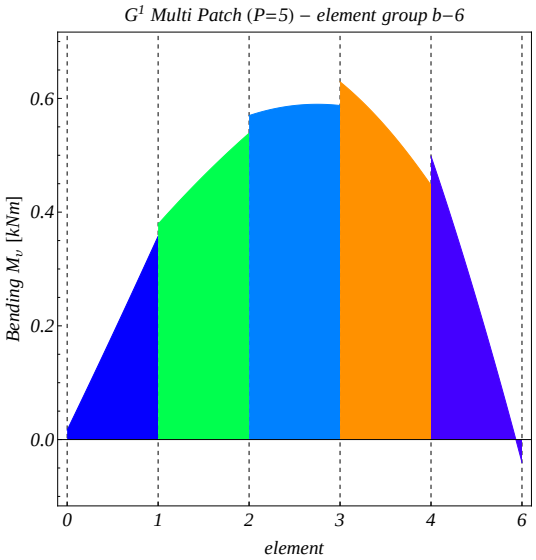

Figure 22: Bending moment M_ν for the element group $b-6$ laying along the x-direction.

5.5.2. Cylindrical grid

The rod axes have been generated considering two families of non geodetic helices on a semi-cylindrical surface, with radius $R = 2.5\,[m]$, with relative distance along the X-direction $p = \frac{R\pi}{4}$, see figure 20(b). The initial normal vector $\hat{\boldsymbol{n}}$ is normal to the surface, so that the intrinsic triad of the of rods is affected by an initial torsion. The dimensions of the rectangular cross section are $h_n = 0.5\,[m]$ and $h_\nu = 0.2\,[m]$, the Young's modulus is $E = 1. * 10^7$, $[kN/m^2]$ and shear modulus $G = 5 * 10^5\,[kN/m^2]$, the point force is $\boldsymbol{F} = \{0, 0, -1\}$, kN. Quintic G^1 Bezier multi-patch elements have been employed. Figure 20(b) shows the initial geometry. Figures 23 shows the deformed configuration obtained. The evaluated vertical displacement at the loaded point is $U_z = -0.0000121782\,[m]$. Figure 24 plots the bending moment M_ν for the helicoidal element group $b - 1$ indicated in figure 20(b). Also in this case there are discontinuities at the patch joints, that are present also in the plots of the axial force and of the torsional moment, not presented here.

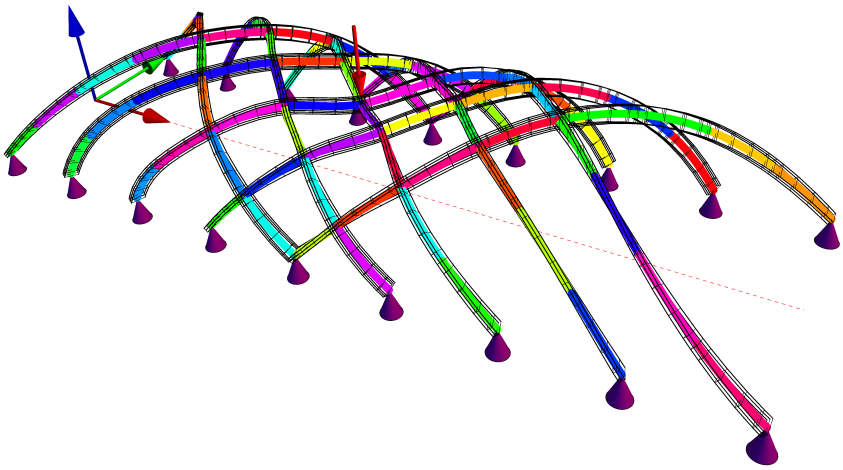

Figure 23: Initial and magnified (MF=20000) deformed configurations for the cylindrical grid.

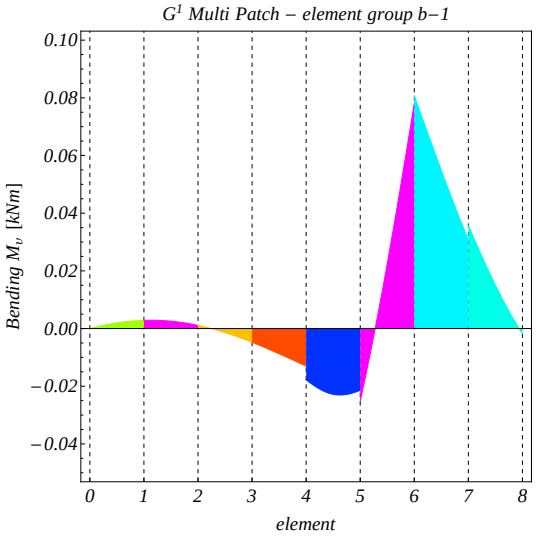

Figure 24: Bending moment M_ν for the helicoidal elements group $b-1$.

6. Conclusions

In the paper has been presented a method for implicitly enforcing G^1 continuity between rod elements discretized using B-splines. The G^1 continuity guarantees the continuity of the bending rotations, while the torsional rotation retains its C^0 continuity introduced by construction of the interpolation. The goal has been reached modifying the degrees of freedom for the control points at the ends of the patch, rather than enforcing the continuity requirements by means of additional constraints. It has been shown that the new parametrization represents a generalization of the Hermite interpolation. Indeed, in the case Bernstein's polynomials of degree 3 are used for the interpolation, the Hermite functions are recovered.

The model of Kirchhoff-Love space curved rods already presented in Greco and Cuomo[27] has been revised, in order to show how the parametrization introduced in the method naturally enforces the required conditions for the rotations at the ends of the element.

Convergence analyses have been presented for different examples, characterized by different types of geometrical coupling between axial, bending and torsional deformation. It is possible to conclude that the G^1 multi-patch approach has the same asymptotic rate of convergence as the single-patch highly continuous B-spline interpolation with $k-$refinement. However the accuracy is lower in the case of the multi-patch approach implemented using Bezier's interpolation in each patch. Adding internal knots in the patch interpolation improves also the accuracy, that tends toward the accuracy of the $k-$refinement, leaving invariant the rate of convergence.

It has also been shown that multi-patch analysis has great benefit in the case concentrated loads (or other types of discontinuities) are present in the structure analysed. In this case highly continuous interpolations produce significant errors, while the multi patch analysis is able to model discontinuities of the required degree. The approach presented in the paper naturally reproduces the physical continuity conditions.

The method proposed has great advantages for modelling complex rod structures like the grids presented in section 5.5, allowing an approach similar to the familiar one used in standard FEM for straight elements.

A promising significant advantage of the proposed formulation has been found examining the behaviour of the error related to the solution as function of the slenderness of the rod. It has been found that, contrarily to what happens for the highly continuous single patch B-spline interpolations, the

multi-patch approach with reduced level of continuity significantly reduces the presence of locking phenomena. This is due to the release of the high continuity constraints present at the rod ends, that are relaxed from C^{p-1} to C^1. These results are illustrated in Greco et al.[41], and a deeper analysis of locking, and of the related phenomena of oscillating solutions, as well as a general strategy for its reduction, will be presented in a forthcoming paper.

As future perspectives, the authors think that the method proposed can be usefully applied to more complex mechanical problems, like models of shells and plates with microstructure, where the continuity of the directors is critical (Neff[42]), or in homogenized models of composite beams with large elongation rigidity and weak bending stiffness, as the one described in Ferretti et al.[43].

References

1. Simo JC, Vu-Quoc L. A three dimensional finite strain rod model. part ii: computational aspect. *Comput Methods Appl Mech Engrg* 1986;58:79–116.

2. Simo J. A finite strain beam formulation. the three dimensional dynamic problem. part i. *Compt Methods Appl Mech Engrg* 1986;42:55–70.

3. Crisfield MA. A consistent co-rotational formulation for non-linear, three-dimensional, beam elements. *Comput Methods Appl Mech Engrg* 1990;81:131–150.

4. Luo AC. On a nonlinear theory of thin rods. *Commun Nonlinear Sci Numer Simulat* 2010;15:4181–4197.

5. Birsan M, Altenbach H, Sadowski T, Eremeyev V, Pietras D. Deformation analysis of functionally graded beams by the direct approach. *Composites: Part B* 2012;43:1315–1328.

6. Antman SS. Nonlinear problem of elasticity. Springer-Verlag, New York; 1995.

7. Langer J, Singer D. Lagrangian aspects of the kirchhoff elastic rod. *SIAM REVIEW* 1995;38:605–618.

8. Ibrahimbegovic A. On finite element implementation of geometrically nonlinear reissnerś beam theory: three-dimensional curved beam elements. *Comput Methods Appl Mech Engrg* 1995;122:11–26.

9. Luongo A, Zulli D, Piccardo G. On the effect of twist angle on nonlinear galloping of suspended cables. *Conmputers & Structures* 2009;87:1003–1014.

10. Bergou M, Wardetzky M, Robinson S, Audoly B, Grinspun E. Discrete elastic rods. *ACM Transactions on graphics* 2008;27(3):63:01–63:12.

11. Jurdjevic V. Non euclidean elastica. *American Journal of Mathematics* 1995;117:93–124.

12. Armero F, Valverde J. Invariant hermitian finite elements for thin kirchhoff rods. i:the linear plane case. *Comput Methods Appl Mech Engrg* 2012;213-216:427–457.

13. Armero F, Valverde J. Invariant hermitian finite elements for thin kirchhoff rods. ii:the linear three-dimensional case. *Comput Methods Appl Mech Engrg* 2012;213-216:458–485.

14. Noels L, Radovitzky R. A new discontinuous galerkin method for kirchhoff-love shells. *Comput Methods Appl Mech Engrg* 208;197:2901–2929.

15. Benson D, Bazilevs Y, Hsu M, Hughes T. A large deformation, rotation-free, isogeometric shell. *Comput Methods Appl Mech Engrg* 2011;(200):1367–1378.

16. Benson D, Bazilevs Y, Hsu M, Hughes T. Isogeometric shell analysis: The reissner-mindlin shell. *Comput Methods Appl Mech Engrg* 2010;(199):276–289.

17. Kiendl J, Bletzinger KU, Linhard J, Wuchner R. Isogeometric shell analysis with kirchoff-love elements. *Comput Methods Appl Mech Engrg* 2009;189:3902–3914.

18. Kiendl J, Bazilevs Y, Hsu MC, Wuchner R, Bletzinger KU. The bending strip method for isogeometric analysis of kirchoff-love shells structures comprised of multiple patches. *Comput Methods Appl Mech Engrg* 2010;199:2403–2416.

19. Gontier C, Vollmer C. A large displacement analysis of beam using a cad geometric definition. *Computer and Structure* 1995;57(6):981–989.

20. Ganapathi M, Patel B, Saravanan J, Touratier M. Shear flexible curved spline beam element for static analysis. *Finite Elements in Analysis and Design* 1999;32:181–202.

21. Nagy AP, Abdalla MM, Gurdal Z. Isogeometric sizing and shape optimization of beam structures. *Comput Methods Appl Mech Engrg* 2010;199(17-20):1216–1230.

22. Lu J, Zhou X. Cylindrical element: Isogeometric model of continuum rod. *Comput Methods Appl Mech Engrg* 2011;200(1-4):233–241.

23. Bouclier R, Elguedj T, Combescure A. Locking free isogeoemetric formulations of curved thick beams. *Comput Methods Appl Mech Engrg* 2012;245-246:144–162.

24. da Veiga LB, Lovadina C, Reali A. Avoiding shear locking for the thimoshenko beam problem via isogeometric collocation methods. *Comput Methods Appl Mech Engrg* 2012;241-244:38–51.

25. Reali A. An isogeometric analysis approach for the study of structural vibrations. *Journal of Earthquake Engineering* 2006;10:1–30.

26. Cottrell JA, Reali A, Bazilevs Y, Hughes T. Isogeometric analysis of structural vibrations. *Comput Methods Appl Mech Engrg* 2006;195:5257–5296.

27. Greco L, Cuomo M. Bspline interpolation for kirchhoff-love space rod. *Comput Methods Appl Mech Engrg* 2012;256:251–269.

28. Piegl L, Tiller W. The NURBS Book. 2 ed.; Springer-Verlag, New York; 1995.

29. Bletzinger KU, Ramm E. Structural optimization and form finding of light weight structures. *Computer & Structures* 2001;79:2053–2062.

30. Fisher P, Klassen M, Mergheim J, Steimann P, Muller R. Isogeometric analysis of 2d gradient elasticity. *Comput Mech* 2011;47:325–334.

31. Greco L. Multi-patch isogeometric analysis of space rods. In: Andrade-Campos A, Lopes N, Valente R, Varum H, eds. *YIC2012-ECCOMAS Young Investigators Conference*. 24-27 April Aveiro, Portugal; 2012:.

32. Cottrell J, Hughes T, Reali A. Studies of refinement and continuity in isogeometric structural analysis. *Comput Methods Appl Mech Engrg* 2007;196:4160–4183.

33. Benson D, Hartmann S, Bazilevs Y, Hsu MC, Hughes T. Blended isogeometric shells. *Comput Methods Appl Mech Engrg* 2013;255:133–146.

34. Farin G. Curve and Surfaces for Computer Aided Geometric Design, A Practical Guide. fifth ed.; Morgan Kaufmann Publishers; 1999.

35. Cottrell J, Hughes T, Bazilevs Y. Isogeometric Analysis: Toward Integration of CAD and FEA. Wiley; 2009.

36. Cuomo M, Greco L. Isogeometric analysis of space rods: Considerations on stress locking. In: Papadrakakis M, Kojic M, Tuncer I, eds. *ECCOMAS 2012 - European Congress on Computational Methods in Applied Sciences and Engineering*; vol. e-Book Full Papers. Wien; 2012:5094–5112.

37. Barsky BA, DeRose TD. Geometric continuity of parametric curves: Three equivalent characterizations. *IEEE Computer Graphics & Applications* 1989;9(6):60–68.

38. Hohmeyer ME, Barsky BA. Rational continuity: Parametric, geometric, and frenet frame continuity of rational curves. *ACM Transactions on Graphics* 1989;8(4):335–359.

39. Echter R, Bischoff M. Numerical efficiency, locking and unlocking of nurbs finite elements. *Comput Methods Appl Mech Engrg* 2010;199:374–382.

40. Cuomo M, Ventura G. An explicit formulation for the greens operator of general monodimensional structures. *European Journal of Mechanics A, Solids* 2002;21:493–512.

41. Greco L, Cuomo M, Impollonia N. An unlocked implicit g^1 continuity multi patch b-spline interpolation for the analysis of 3d kirchhoff-love rod

elements. In: Papadrakakis M, Kojic M, Tuncer I, eds. *SEECCMIII,* 3^{th} *South-European Conference on Computational Mechanics*. 12-14 June, Kos Island, Greece; 2013:.

42. Neff PA. A geometrically exact cosserat shell model including size effects, avoiding degeneracy in the thin shell limit. *Continuum Mechanics and Thermodynamics* 2004;16(6):577–628.

43. Ferretti M, Madeo A, dellIsola F, Boisse P. Modelling the onset of shear boundary layers in fibrous composite reinforcements by second gradient theory. *ZAMP Zeitschrift fr angewandte Mathematik und Physik* 2013;(doi.org/10.1007/s00033-013-0347-8).